Cell

Article

A brainstem integrator for self-location memory and positional homeostasis in zebrafish

Graphical abstract

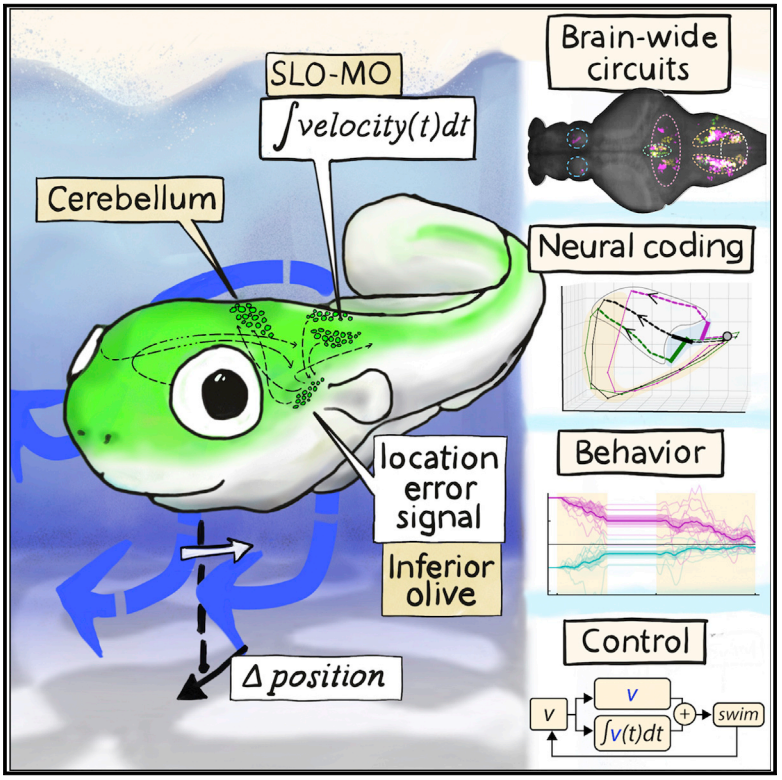

Highlights

- Larval zebrafish can remember self-location to control their position in space
- Control theory models place algorithmic constraints on the neural controller
- Neurons in brainstem and cerebellum encode the memory and control algorithm
- Perturbation experiments causally link these neurons to goal-directed behavior

Authors

En Yang, Maarten F. Zwart, Ben James, ..., Brett D. Mensh, James E. Fitzgerald, Misha B. Ahrens

Correspondence

yange@janelia.hhmi.org (E.Y.), ahrensm@janelia.hhmi.org (M.B.A.)

In brief

Whole-brain functional imaging of larval zebrafish reveals a multiregional brainstem and cerebellar circuit that integrates self-motion and stores self-location to control corrective fictive swimming in response to involuntary displacements.

Yang et al., 2022, Cell *185*, 5011–5027
December 22, 2022
https://doi.org/10.1016/j.cell.2022.11.022

CellPress

Cell

CellPress
OPEN ACCESS

Article

A brainstem integrator for self-location memory and positional homeostasis in zebrafish

En Yang,[1,*] Maarten F. Zwart,[1,2] Ben James,[1] Mikail Rubinov,[1,3] Ziqiang Wei,[1] Sujatha Narayan,[1] Nikita Vladimirov,[1,4] Brett D. Mensh,[1] James E. Fitzgerald,[1] and Misha B. Ahrens[1,5,*]

[1]Janelia Research Campus, Howard Hughes Medical Institute, Ashburn, VA 20147, USA
[2]School of Psychology and Neuroscience, Centre for Biophotonics, University of St Andrews, St. Andrews, UK
[3]Department of Biomedical Engineering, Vanderbilt University, Nashville, TN 37235, USA
[4]URPP Adaptive Brain Circuits in Development and Learning (AdaBD), University of Zurich, Zurich, Switzerland
[5]Lead contact
*Correspondence: yange@janelia.hhmi.org (E.Y.), ahrensm@janelia.hhmi.org (M.B.A.)
https://doi.org/10.1016/j.cell.2022.11.022

SUMMARY

To track and control self-location, animals integrate their movements through space. Representations of self-location are observed in the mammalian hippocampal formation, but it is unknown if positional representations exist in more ancient brain regions, how they arise from integrated self-motion, and by what pathways they control locomotion. Here, in a head-fixed, fictive-swimming, virtual-reality preparation, we exposed larval zebrafish to a variety of involuntary displacements. They tracked these displacements and, many seconds later, moved toward their earlier location through corrective swimming ("positional homeostasis"). Whole-brain functional imaging revealed a network in the medulla that stores a memory of location and induces an error signal in the inferior olive to drive future corrective swimming. Optogenetically manipulating medullary integrator cells evoked displacement-memory behavior. Ablating them, or downstream olivary neurons, abolished displacement corrections. These results reveal a multiregional hindbrain circuit in vertebrates that integrates self-motion and stores self-location to control locomotor behavior.

INTRODUCTION

Many animals keep track of where they are in their environment.[1] Self-location information is important for many behaviors,[2] such as efficiently returning to safe locations after visiting unknown and potentially dangerous areas, revisiting food-rich areas, and avoiding foraging in food-poor areas. These navigational abilities are thought to be supported by neural representations of self-location[3–7] in the hippocampus of mammals[8–10] or its homolog in fish,[11–13] entorhinal cortex,[14,15] and retrosplenial cortex,[16] as well as by representations of heading in subcortical neural integrators[17–19] and the central complex of *Drosophila melanogaster*.[20–22]

Self-localization relies upon multiple cues, including environmental and proprioceptive sensations generated by self-movement.[23–29] Navigational behaviors in ants,[30] mammals,[31,32] and fruit flies[33] involve a fundamental neural computation called path integration, whereby animals estimate their location by integrating their movements. An important cue for path integration is optic flow because the speeds and directions of motion signals across the retina provide information about an animal's motion through its environment.[34–40] Extracting self-velocity from optic flow arising from self-generated movements (e.g., swimming, walking, and flying) and movements imposed by the environment (e.g., fish moved by water flow or birds by wind) and integrating it over time[41] produces a representation of how much and in which direction an animal has moved. In mammals, path integration is thought to rely on computations in entorhinal networks that combine multimodal information.[5,15,29,42,43] However, unknown positional integrators could contribute to goal-directed behavior.

Unexpected circuits have been difficult to discover because neuroscience typically relies on recordings from cells in preselected brain regions that cover a small fraction of all neurons in the brain. We therefore sought to identify complete navigational circuits in larval zebrafish (*Danio rerio*), from motion integrators to premotor centers, by imaging and analyzing the entire brain at cellular resolution during a behavior that relies on self-localization. Access to over 100,000 neurons per animal revealed brain regions that had not been known to be involved in self-localization, leading to the discovery of a multiregional hindbrain circuit mediating a transformation from velocity, through displacement memory, to behavior.

We studied a behavior in which larval zebrafish remember past displacements to maintain their approximate location in space. Fish can turn and swim toward water flow via mechanosensory rheotaxis behavior[44,45] and the visual optomotor (OMR) response.[36–38,46,47] However, it is unknown whether they track their location over long timescales and use memorized positional information to bias future swimming, allowing them to move closer to their earlier location. Such capabilities can be

ethologically critical because larval zebrafish swim intermittently[48,49] and are moved by currents during rest, potentially into dangerous locations. Here, we demonstrate that larval zebrafish counteract unintended displacements by altering their future swimming to later return to the locations where they would have been without the displacement (a behavior we term positional homeostasis) and uncover its neural implementation in a multiregional circuit in the hindbrain. This circuit involves the inferior olive (IO) and cerebellum, thereby connecting self-localization and olivocerebellar motor control.[50] This multiregional circuit has potential anatomical and functional homologs in mammals and may interact with other known representations of self-location. This work establishes the vertebrate hindbrain as a neural control center for behaviors requiring navigation.

RESULTS

Zebrafish counteract past involuntary displacements over tens of seconds

When landmarks are not available, accurate positional homeostasis requires path integration, which combines the direction and magnitude of instantaneous velocity over prolonged time periods to compute overall displacement. We exploited a well-known behavior, in which many fish species swim against water currents. Larval zebrafish exposed to various virtual currents can approximately steady their location in space, despite swimming only a fraction of the time (e.g., Figure S1A; a swim bout lasts ~100–400 ms with gaps of a second or longer between bouts). Fish swam and controlled their visual feedback in a closed-loop, one-dimensional, virtual-reality (VR) environment[51] with fine stripes or random visual patterns (Figure 1A). Larval zebrafish swim forward when they perceive forward visual motion,[38,46] thereby reducing their net displacement in environments with water currents that would otherwise move them backward (Figure 1B).

Based on this innate behavior, we constructed a behavioral assay to test if fish have an internal representation of self-location (Figure 1C). This assay is based on the idea that if a fish's location is unexpectedly changed (e.g., by environmental factors like a sudden stream of water), fish may correct for it by swimming back to their earlier location. If they do so robustly, then finding a representation of location in their brain may be possible. In each trial, the fish started at a specific zero-location, which was determined by the fish itself during a preceding period in which it swam in VR (see below). Next, its position was changed in a "pre-displacement period" to a location determined by one of several pre-programmed trajectories that the fish could not control[52] (ending in a total displacement multiple times its ~4 mm body length). These trajectories were chosen so that the fish would swim little, or not at all, by using only short periods of translation and limiting how much the fish was displaced backward (fish may require a threshold displacement before they start corrective swimming). A "zero pre-displacement trajectory" was the baseline for comparison. The fish was then held at the same location for several seconds in a "delay period." Both the pre-displacement and the delay periods are in open loop, so that if a fish does swim, it does not trigger any motion through VR. In the subsequent "swim response period," the fish was exposed to a prolonged virtual backward current and free to swim forward in a closed loop, such that swimming triggered forward motion through VR. Although fish cannot swim backward in VR, with backward flow, they can choose to reposition backward or forward depending on how much they swim. The balance between backward flow velocity and the amount of forward swimming determined the fish's final position. This final position formed the starting position of the next trial; hence, the starting location of each trial was determined by the fish.

We asked whether fish compensated for pre-displacement by analyzing whether the swim-period trajectory converged with the zero-displacement trajectory or remained separated by the amount of earlier passive displacement. For instance, a fish simulated as a memoryless control system that only responds to instantaneous visual flow could swim to counteract the motion, but average trajectories for forward-, zero-, and backward pre-displacement trials would remain separated (Figure 1D, top). In contrast, a fish simulated as a control system with perfect spatial memory (a type of proportional-integral-derivative [PID] controller[53]; STAR Methods) could respond to flow but also swim to cancel earlier displacements. Thus, average trajectories for forward, zero, and backward pre-displacements would converge (Figure 1D, bottom). In real fish, swim trajectories approximately converged: after forward or backward pre-displacements, on average, fish reached locations consistent with zero pre-displacement trajectories after about 10 s of swimming (Figures 1E and 1F; Figures S1B and S1C). Because the trajectories continue to converge until the end of the 10-s swim period after the 5-s delay period, this result implies that fish retain an accurate memory of the pre-displacement for at least 15 s.

Trajectory convergence was a robust feature of fish behavior that occurred in a wide range of experimental protocols. For example, fish were able to correct for more complex pre-displacements, such as multiple displacements or displacements of different durations (Figures S1D–S1G). They also corrected for pseudo-random forward and backward trajectories followed by a swim period that was broken in two (Figures 1G and 1H), so that the convergence continued over 20 s. Behavioral effects induced by pre-displacements included modulation of response time and swim vigor in the swim period (Figures S1H–S1J). Trajectories also converged following a change in motosensory gain, showing that fish use visual flow for positional homeostasis even when swim outcomes (amount of translation per unit of swimming) are altered, consistent with visually driven path integration (Figures S1K–S1N). Trajectories also converged if the flow velocity during the swim period was different from the velocity of the pre-displacement (Figures S2A–S2C). Furthermore, trajectory convergence could occur whether or not fish swam prior to the swim period (Figure S2D). Trajectory convergence did not require landmarks nor did it require the visual scene to remain visible during the delay period (Figure S2E). Thus, fish integrate visual flow into a representation of location change and correct for unintended location changes by altered swimming, with location memories persisting longer than 20 s.

Fish showed slow forward or backward positional drift during the closed-loop swim period in all trial types (Figures S3A and S4A). Such drift may be due to motivated behaviors that are independent of positional stabilization, but drift can also occur in control systems that are targeted at positional stabilization (Figures

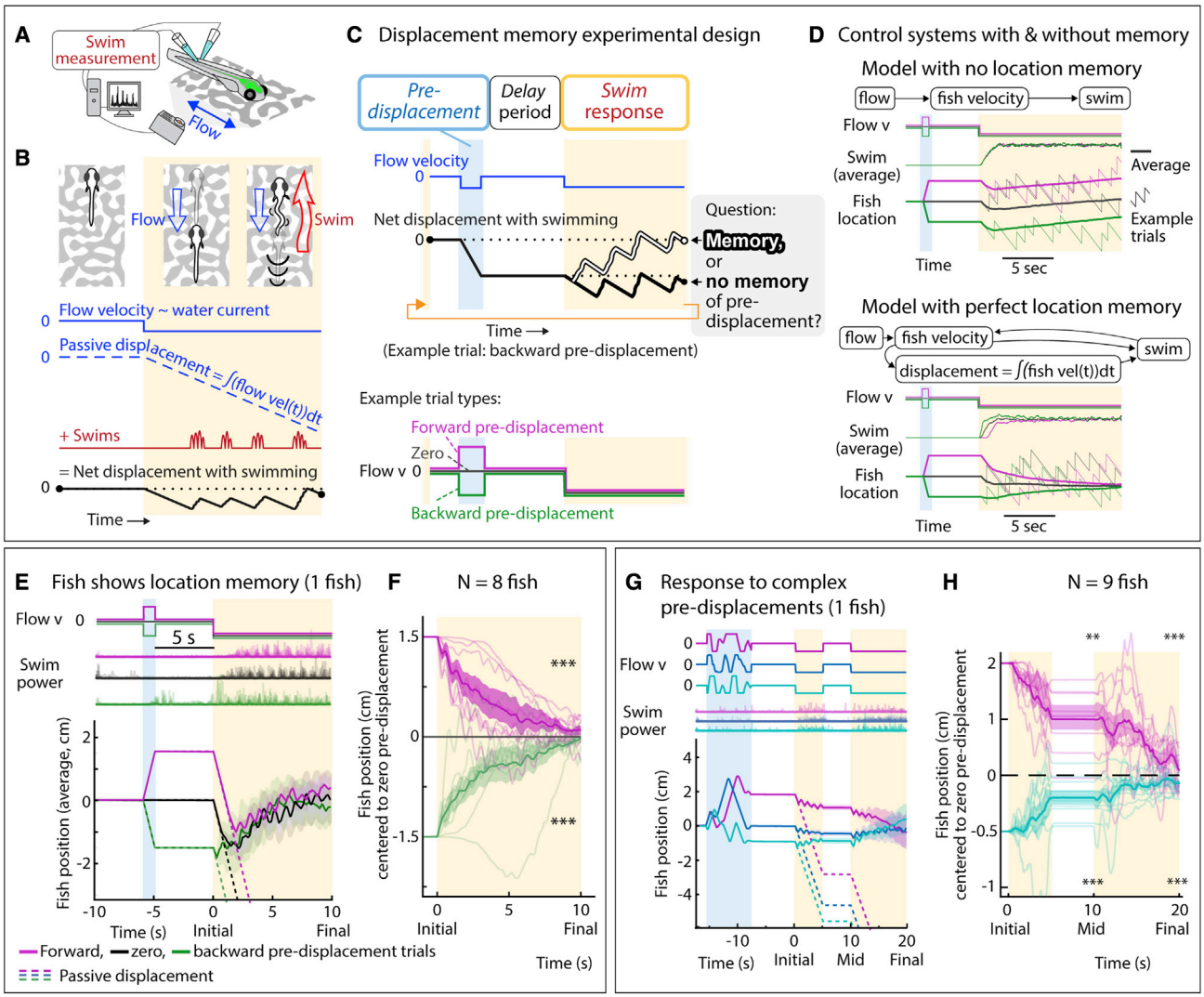

Figure 1. Larval zebrafish track their spatial location and correct for unintended displacements

(A) Experimental setup: larval zebrafish fictively swimming in a virtual reality environment.

(B) Fish swim in response to virtual flow so that their net displacement is smaller than the passive displacement. Dashed lines show passive displacements here and in later figures.

(C) Experimental design: fish undergo one of various forced trajectories (blue pre-displacement period). After a delay period (white), they can correct for the pre-displacement by swimming the correct amount against a virtual flow in "closed loop" (yellow swim period).

(D) Simulated fish behavior showing two classes of outcomes. If average trajectories during forward versus backward pre-displacements converge during the swim period, it implies fish have memory of self-location.

(E) Example fish behavior in pre-displacement experiment. Average trajectories for the three trial types approximately converge at ~5 s, showing that this fish has memory of pre-displacement. (Shaded regions, SEM in all panels.)

(F) Trajectories (8 fish) normalized and centered to zero pre-displacement trajectory converge at ~10 s, indicating accurate memory of previous location shift. (One-sample t test for final positions, ***$p < 0.001$, $p = 7.3e{-}8$ for backward pre-displacement, specified mean = −1; $p = 6.3e{-}7$ for forward pre-displacement, specified mean = 1.)

(G) Assay to test integration during stochastic pre-displacements and to examine corrections made over two swim periods separated by a delay. This example fish successfully corrects for stochastic pre-displacements; correction continues across two swim periods.

(H) Population data showing accurate correction distributed over both swim periods, i.e., 1D path integration of complex trajectories. (One-sample t test, **$p < 0.01$, $p = 0.0023$ for forward pre-displacements at mid time point, ***$p < 0.001$, $p = 2.5e{-}5$ for backward pre-displacements at mid time point. $p = 2.1e{-}7$ for forward pre-displacement at final time point, $p = 5.8e{-}8$ for backward pre-displacement at final time point. Data shown centered to average of trajectories that integrate to zero.).

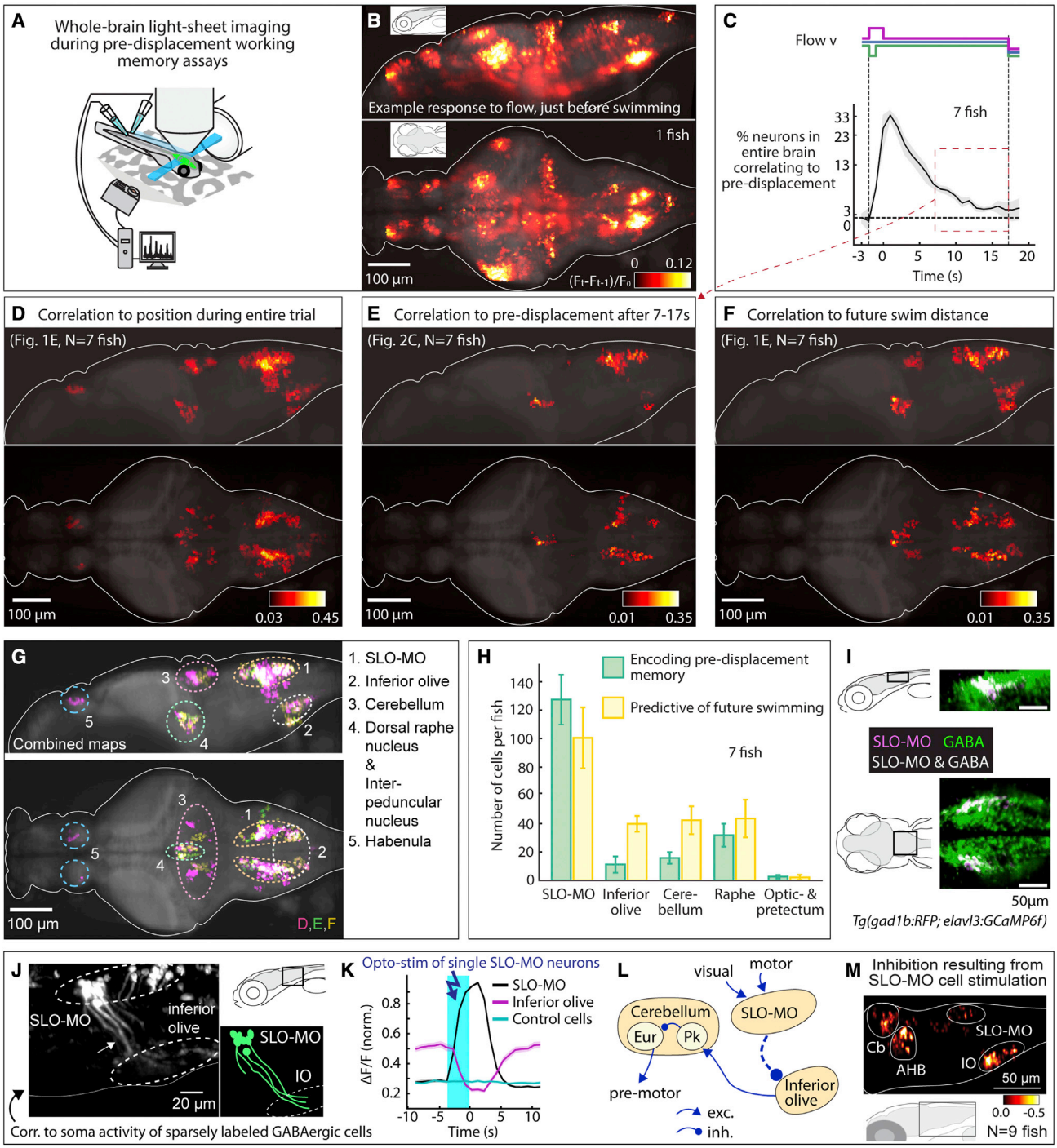

Figure 2. Whole-brain activity maps reveal neural populations encoding self-location

(A) Virtual reality system for paralyzed zebrafish and light-sheet microscope for imaging whole-brain cellular activity.

(B) Example brain-wide activity following forward visual motion, just before swim initiation in *Tg(elavl3:GCaMP6f)* fish (Figure S5A for earlier and later time points). Shown is the difference between imaging frames F_{t-1} and F_t normalized by baseline fluorescence, where F_{t+1} are frames containing the first swim bouts occurring after swim period onset.

(C) Fraction of neurons across the brain with significant correlation to pre-displacement direction as a function of elapsed time. At 17 s after the pre-displacement, a fraction of neurons still encodes pre-displacement direction (shaded regions: SEM; arrow refers to time period used for analysis in (E); backward pre-displacement is shorter than forward to limit swimming during pre-displacement).

(legend continued on next page)

S4B–S4F). In particular, gradual drift is consistent with a PID-style control system in which a weighted sum of instantaneous velocity and a "leaky" integral of velocity (i.e., position estimate) determine swimming (Figure S4B; see STAR Methods). In such systems, as the location memory slowly degrades, the effective zero position of the system can shift forward or backward (see STAR Methods for mathematical details; simulations in Figures S4B–S4D). The precision of location memory is determined by the leakiness of velocity integration and is reflected in trajectory convergence after different pre-displacements, where greater convergence implies greater memory (Figures S4C–S4F).

Positional drift can also occur if location memory is precise but the fish has estimated its velocity incorrectly.[54] In our formulation, the fish is assumed to have perfect knowledge of the true drift velocity, whereas in actuality, the velocity must be estimated from visual information. Slow drift occurred more often in the presence of the blue light sheet during imaging, suggesting that drift may partially reflect noisy visual computations or an imperfect relay of the velocity signal by the visual system that leads to an underestimate of flow, as seen in other species.[55] Regardless of the source of this slow drift, our mathematical model and the observed trajectory convergence suggest that fish have an accurate location memory consisting of a leaky velocity integrator with a long time constant (Figure S4E).

Brainstem codes for self-location

To identify brain regions encoding self-location, we used whole-brain light-sheet microscopy[56–58] to record single-neuron activity using genetically encoded calcium indicators (Figures 2A and 2B; Figure S5A). To search for activity encoding displacements that occurred many seconds ago, we exposed fish to a forward or backward pre-displacement followed by a 17-s delay period. We found neurons whose activity correlated with the positional shift for the entire delay period (Figure 2C; STAR Methods), suggesting that the brain persistently encodes past displacements.

To investigate location encoding and its transformation to behavior, we analyzed whole-brain activity of fish in virtual reality assays for (1) cell activity that correlated to position during the entire trial (with 10-s pause; STAR Methods), (2) cell activity that correlated with positional shifts in long delay periods (using 17-s delay as above), and (3) cells whose activity at swim period onset correlated with how far the fish swam in the swim period (STAR Methods). These analyses produced three whole-brain activity maps (Figures 2D–2F) that were used to guide functional analyses and perturbation experiments to pinpoint causal mechanisms.

The brain regions thus revealed were consistent across these maps (Figure 2G). (Some consistency in the maps is expected because the statistical measures used to construct them are not independent.) The results from individual fish were largely in agreement with the combined maps (Figures S5B–S5E). We named the most populous cluster of neurons, in the dorsal hindbrain, as Self-LOcation encoding Medulla Oblongata neurons (SLO-MO; Figures 2D–2G). Smaller clusters were present in the IO,[60,61] cerebellum,[61,62] dorsal raphe nucleus (DRN),[63] the area of the interpeduncular nucleus (IPN),[19] and habenula (Figures 2D–2G). The IPN and habenula clusters became uncorrelated to the pre-displacement at the end of the long (17 s) delay period, and the habenula was not significantly correlated to future swimming (Figures 2E and 2F). The pallium, which has been proposed to contain the homologue of the hippocampus,[13] in some fish contained activity that correlated to location, but this was not consistent across animals (Figures S5B–S5E and S5H). We quantified which of the remaining regions contained neurons that correlated with pre-displacement memory or future swim distance. SLO-MO contained most memory-correlating neurons, along with a smaller number of neurons that correlated with future swim distance (Figure 2H). The inferior olive (IO) and cerebellum also contained both types but had more neurons correlated with future swimming (Figure 2H). The DRN contained both types in similar amounts (Figure 2H), although it encoded forward but not backward pre-displacements (Figure S5H). For comparison, we found neither neuron type with similarly long-timescale integration in optic tectum (OT) or pretectum (PT) (Figure 2H).[40,64–66] Thus, the analysis of whole-brain functional data provides a specific set of brain areas for further investigation.

These response properties led us to hypothesize that a SLO-MO⇢IO→Cb pathway underlies the transformation from displacements to corrective future swimming (⇢: functional connection; →: known monosynaptic connection). To investigate SLO-MO's cell types and functional connections, we used

(D) Whole-brain map of neurons encoding self-location during pre-displacement, delay, and swim periods. Cells with $p < 0.005$ for Spearman correlation in at least 80% of time points are shown (STAR Methods). Color bar represents averaged Spearman correlation coefficient to location.
(E) Map of neurons encoding self-location during long delay period (C). Cells with $p < 0.005$ for Spearman correlation to self-location at every time point between 7 and 17 s are shown. Color bar represents averaged Spearman correlation coefficient of all time points.
(F) Map of neurons whose activity at swim period onset (before first swim bout) predicts total distance swum in swim period. Cells with $p < 0.005$ for Spearman correlation at first two time points in the swim period are shown. Color bar represents averaged Spearman correlation coefficient.
(G) Combined maps of (D)–(F) listing brain areas containing neurons potentially involved in self-localization.
(H) Numbers of identified neurons (cell segments) per fish per area encoding memory of location during pre-displacement and delay periods, and numbers of neurons predicting future distance swum in the swim period. (Error bars, SEM.)
(I) Dorsal hindbrain map of SLO-MO neurons and GABAergic neurons in *Tg(elavl3:GCaMP6f; gad1b:RFP)* showing strong overlap between SLO-MO and GABAergic populations (white).
(J) Hybrid functional and anatomical tracing of SLO-MO neurites through sparse expression in *Tg(gad1b:Gal4; UAS:GCaMP6f)* using fluorescence correlation to SLO-MO cell body activity to help distinguish neurites in sparse gad1b line, showing innervation of IO (STAR Methods).
(K) Optogenetic activation SLO-MO (single neurons of any functional type; STAR Methods) using CoChR[59] in *Tg(gad1b:Gal4; UAS:CoChR; elavl3:jRGECO1b)* (see Figures S7K and S7L) shows IO neurons are inhibited during SLO-MO activation, indicating functional connection consistent with GABAergic inhibition.
(L) Local circuit diagram of hypothesized SLO-MO inhibition of IO (dashed line) and known circuitry from IO to Cb cell types (Pk, Purkinje cells; Eur, eurydendroid cells, homologous to deep cerebellar nuclei).
(M) Hindbrain functional map of decreases in cell activity (color bar, relative decrease $\Delta F/F$) during SLO-MO activation (one neuron at a time) showing activity reduction in IO, cerebellum, anterior hindbrain (AHB), and non-stimulated SLO-MO cells.

transgenic fish lines with GCaMP6f[67] or jGCaMP7f[68] expressed in all neurons and a red co-label in cells with specified neurotransmitters. Most SLO-MO cells were GABAergic (Figure 2I). To trace their projections, we expressed GCaMP in a sparse subset of GABAergic neurons and imaged them in the pre-displacement assay. By correlating imaged voxels with ΔF/F signals from functionally identified SLO-MO cells, we identified projections to the area of IO dendrites[69] (Figure 2J), suggesting that SLO-MO may monosynaptically inhibit IO. To test for functional coupling, we optogenetically stimulated functionally identified SLO-MO cells while imaging IO cells and found that IO activity was inhibited when SLO-MO was stimulated (Figure 2K). Thus, SLO-MO, IO, and thereby cerebellum are functionally connected (Figure 2L). We hypothesize that these regions contain the core circuit underlying the representation of self-displacement and its transformation to corrective locomotion. Whole-hindbrain imaging during SLO-MO stimulation (Figure 2M) revealed inhibited cells in the IO, cerebellum, and anterior hindbrain (AHB). IO and cerebellum are involved in sensorimotor control,[70–72] and AHB codes sensorimotor cues relevant for OMR behavior[35-37,73]; hence, this result raises the possibility that modulation of IO activity by SLO-MO cells allows fish to combine memories of past positional shifts with responses to new visual flow.

To investigate the transformation from memory to action, we first analyzed how SLO-MO activity represents self-location in the pre-displacement assay. Two broad neuron classes contained information about fish location (Figure 3A): activity in one class persistently increased following backward pre-displacement (Figure 3B), whereas activity in the other increased following forward pre-displacement (Figure 3C). (This persistent activity far outlasted the ~2 s decay time constant of the calcium indicator.) Even during zero pre-displacement trials, many neurons had nontrivial dynamics, such as ramping up or ramping up then down, during the delay period (Figures 3B and 3C, black traces; any apparent response at the start of the delay period of the top-left cell in Figure 3B is likely coincidental, as other cells generally do not show such a pattern). Relative to this zero-displacement activity, activity of the first neuron class increased when fish were displaced backward (Figure 3B, bottom), whereas activity of the second class did the opposite (Figure 3C, bottom). Average activity over SLO-MO cells in these classes showed that location encoding decays slowly over about 20 s (Figures 3B and 3C, bottom). Visualized in dimensionally reduced principal-component space, trial-averaged SLO-MO population trajectories split into three branches, corresponding to backward, zero, and forward pre-displacement trials, which remained separated during the delay period, then converged during the swim period as fish trajectories converged, and returned to near the starting point (Figure 3D; Figures S6A and S6B). The zero-pre-displacement trajectory is not stationary during the delay period because of the nontrivial dynamics of SLO-MO. Swimming affected these dynamics, as SLO-MO cells showed a transient decrease in activity during swimming but returned to normal activity levels a few seconds later (Figures S6C–S6F). This robust pre-displacement encoding is reminiscent of attractor dynamics.[74]

Thus, representations of position are encoded within neural activity. Across nine fish (1,347 SLO-MO neurons), SLO-MO cell activity correlated to fish location for over 15 s after displacement (Figure 3E; Figures S6E and S6F). Such persistent correlations were absent in two control neuronal populations: (1) motor-correlated hindbrain neurons on trials where the fish did not swim during the pre-displacement and delay periods (Figure 3F) and (2) pretectal neurons (Figure 3G). Persistent effects of displacement were also visible in average activity of forward/backward-tuned neural populations across fish (Figure 3H). SLO-MO neurons also represented location during more complex random trajectories (Figure 3I) and other trajectory types (Figures S6G–S6J), showing that they integrate velocity into a representation of position across a large range of velocity profiles, and this integrated value persists for many seconds in the absence or presence of swimming. This relationship is also visible at the single-spike level (Figure S6K). SLO-MO activity typically decreases during the swim period (Figure S3B), consistent with the convergence of the average trajectories. However, SLO-MO decay can also occur when drift causes the fish's position to change, which suggests that the slow positional drift does not get encoded in SLO-MO due to the integration leak or sensory noise. Cells in the SLO-MO region could encode sideways shifts (Figure 3J), suggesting that the population code generalizes to 2D locations in space. We conclude that across a variety of trajectory types, SLO-MO neurons persistently encode self-location.

SLO-MO position-encoding coexists with complex background dynamics, including spontaneous ramping and decay dynamics (Figures 3B and 3C) and transient behavior encoding (Figures S6C–S6F). We wondered whether a simple fixed decoder could nevertheless read out fish location. We trained a set of linear decoders that predicted a fish's location as a weighted sum of its neuronal activity at a given time (Figure 4A). Each linear decoder predicted fish location during random motion sequences and the delay period (Figures 4B and 4C, all on held-out trials). Decoding fidelity decreased over time (compare Figure 4D left to right). For comparison, decoders trained on visual midbrain neurons performed poorly (Figure 4E). The decoder could predict activity on individual trials (Figure 4F), including during swim periods where the fish controlled its position. Decoding was accurate across the fish population during (Figure 4G) and at the end of trials (Figure 4H, 20 s after the initial displacement). Thus, SLO-MO activity robustly encoded fish location based on integrated optic flow.

SLO-MO integrates motion, is necessary for positional homeostasis, and changes future locomotion

We used two-photon ablation to test whether SLO-MO neurons are necessary for the neural and behavioral memory of displacements (Figure 5A). To do so, we imaged responses to pre-displacements, used online analysis to identify SLO-MO neurons (STAR Methods[75]) and ablated either all SLO-MO neurons identified as positively encoding a backward pre-displacement or all neurons positively encoding a forward pre-displacement at single-cell resolution (Figures S7A–S7C). Despite some topography, in most fish, these functional populations were intermingled, bilateral, and in close proximity (e.g., Figure 5B; Figure S7E, inset). Ablating either population disabled the persistence of visual responses in the other (Figures 5B and

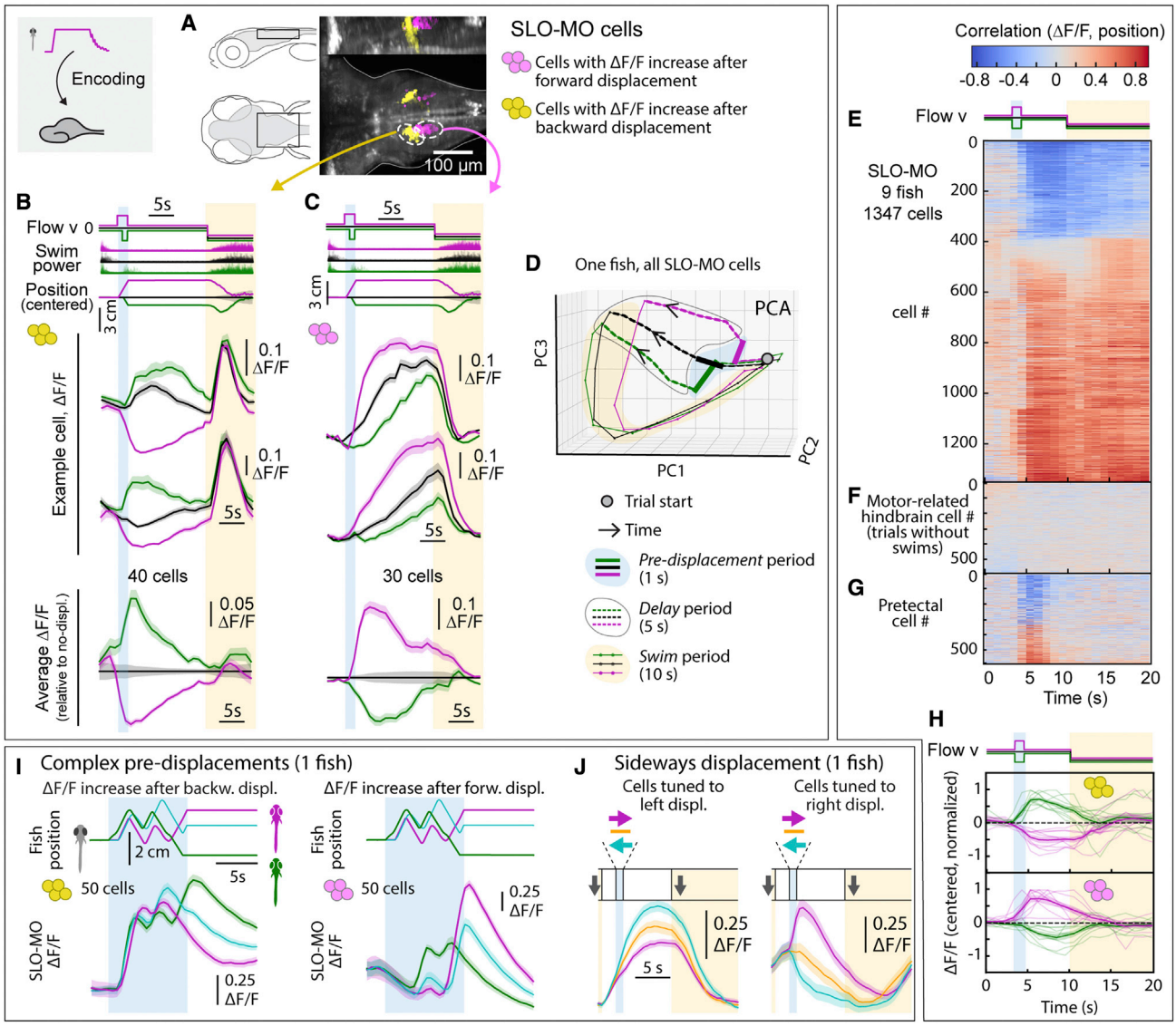

Figure 3. SLO-MO neuronal activity encodes self-location

(A) Location of neurons with increasing activity following backward (yellow) versus forward (magenta) pre-displacement in example fish.

(B) Examples (top) and average (bottom, with ΔF/F during no-displacement trials subtracted) of neurons with increasing activity following backward pre-displacement. (Shaded regions: SEM in all panels; here, 2 s forward or 1 s backward pre-displacements.)

(C) Examples (top) and averages (bottom) of neurons with increasing activity following forward pre-displacement.

(D) Principal-component analysis embedding of SLO-MO population activity. Trajectories remain separated throughout delay period, gradually converge and return toward the starting point during swim period.

(E) SLO-MO neuron activity across 9 fish (1,347 cell segments) sorted by Spearman correlation, showing consistent correlation to self-location across trial types.

(F and G) For comparison, lack of correlation to self-location for cells with activity correlating to swim vigor, and for cells in pretectum that show visual encoding.

(H) Averages of ΔF/F (centered to zero pre-displacement, normalized in each fish) of positive- and negative-correlating neurons from (E).

(I) Encoding of self-location by SLO-MO neurons during complex trajectories (example fish).

(J) Encoding of sideways changes in self-location in SLO-MO neurons (example fish).

5C). That is, visual responses in the remaining population were still present after ablation, but they were no longer persistent (Figure 5C; Figures S7D–S7G). This result suggests that integration of optic flow on timescales longer than ~5 s occurs in SLO-MO instead of being inherited from an upstream region and that integration occurs via local connectivity within SLO-MO.[76–79]

Behaviorally, post-ablation fish no longer corrected for pre-displacements in either direction (Figures 5D and 5E; Figure S7H), no matter which population was ablated. Fish still responded to visual flow (e.g., swimming in Figure 5D), and control ablations of nearby non-SLO-MO neurons did not affect spatial memory (Figure 5E). Thus, SLO-MO lesions abolish displacement

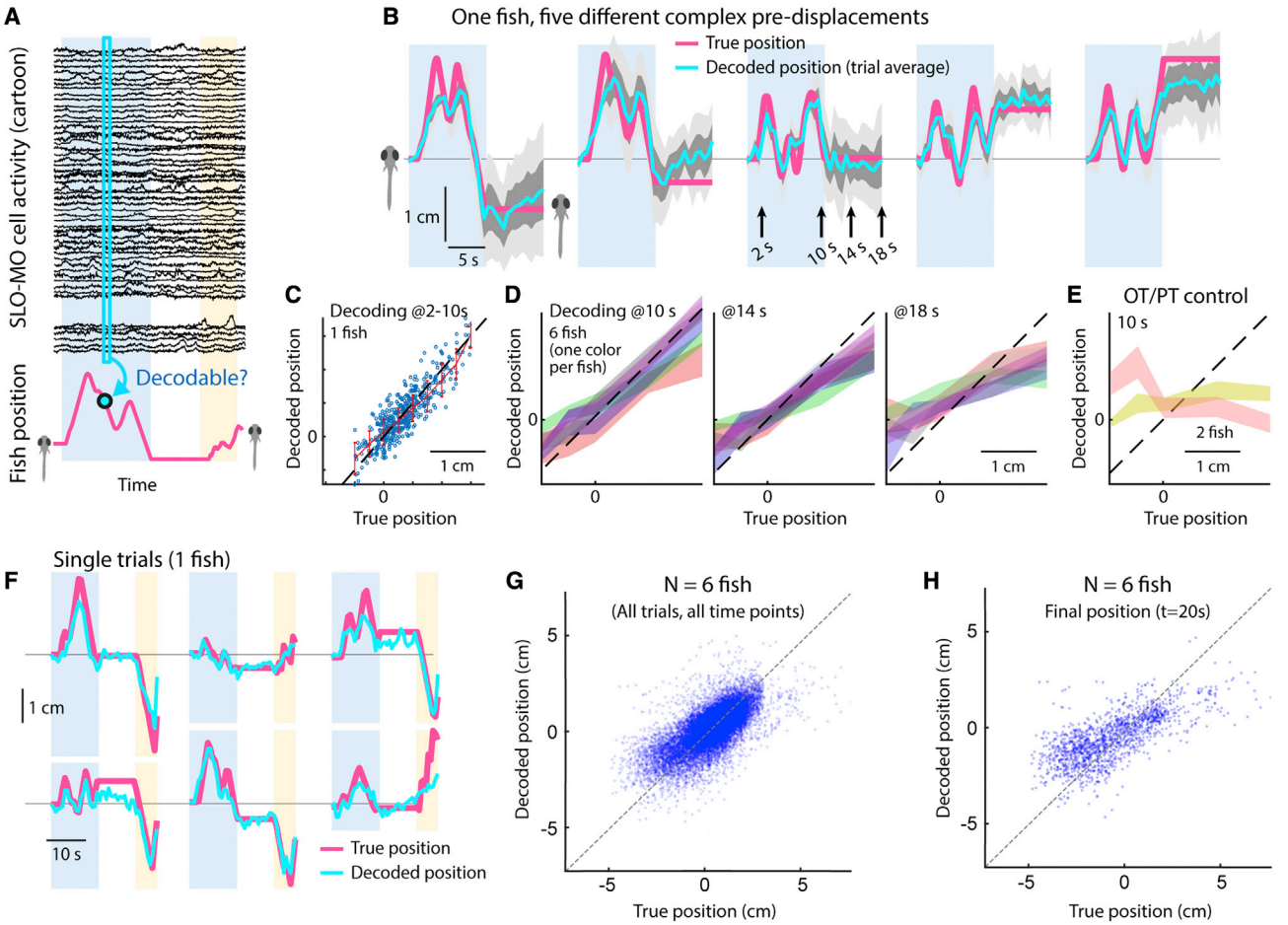

Figure 4. Decoding self-location from SLO-MO neuronal activity

(A) Schematic of self-location decoding from SLO-MO population activity (cartoon data).

(B) Decoding averages of complex location trajectories in pre-displacement and delay periods of stochastic displacement assay (dark gray: standard error [SEM], light gray: standard deviation [SD]). (Fish icons enlarged, not to scale.)

(C) Decoding performance throughout pre-displacement period of example fish.

(D) Decoding performance at start, middle, and end of delay period across N = 6 fish, showing gradually declining performance as SLO-MO memory decays over many seconds (colors: SEM for each fish).

(E) Decoder trained on midbrain visual neurons performs poorly.

(F) Example decoding of single trials, including first swim period.

(G) Decoding self-location during entire trial across N = 7 fish, $r = 0.54$, $p < 0.01$.

(H) Performance of decoding self-location at end of swim period (at $t = 20$ s), $r = 0.68$, $p < 0.01$.

memory older than ~5 s. Although other integrators of visual motion on shorter timescales may persist after such lesions, we conclude that SLO-MO integrates motion into persistent activity for tens of seconds and is necessary to maintain displacement memory longer than ~5 s.

To test if SLO-MO activity influences future swimming, we optogenetically activated a subset of SLO-MO neurons (~3–7 per fish) that all either encoded forward, or all encoded backward pre-displacements with an activity increase (Figure 5F). After a 5-s delay, fish behavior during the swim period was altered as if an actual displacement had occurred in the direction encoded by the stimulated population (Figures 5G and 5H; Figures S7I and S7J). Control stimulations of nearby non-SLO-MO GABAergic neurons did not have such effects (Figure 5H, right). Thus, activation of SLO-MO subpopulations mimics the behavioral effects of true displacement memory. Moreover, a transient optogenetic pulse led to long-lasting behavior effects, reinforcing the conclusion that path integration contributes to the computation of displacement memories in SLO-MO because there are no sustained cues that could mimic environmental landmarks. Based on this result and the near-complete elimination of memory after SLO-MO ablation, we conclude that SLO-MO is a major locus of spatial location memory in our behavioral assays.

IO is modulated by SLO-MO and is necessary for positional homeostasis

To probe the relationship between SLO-MO and IO activity, we used dual-color functional imaging to simultaneously record

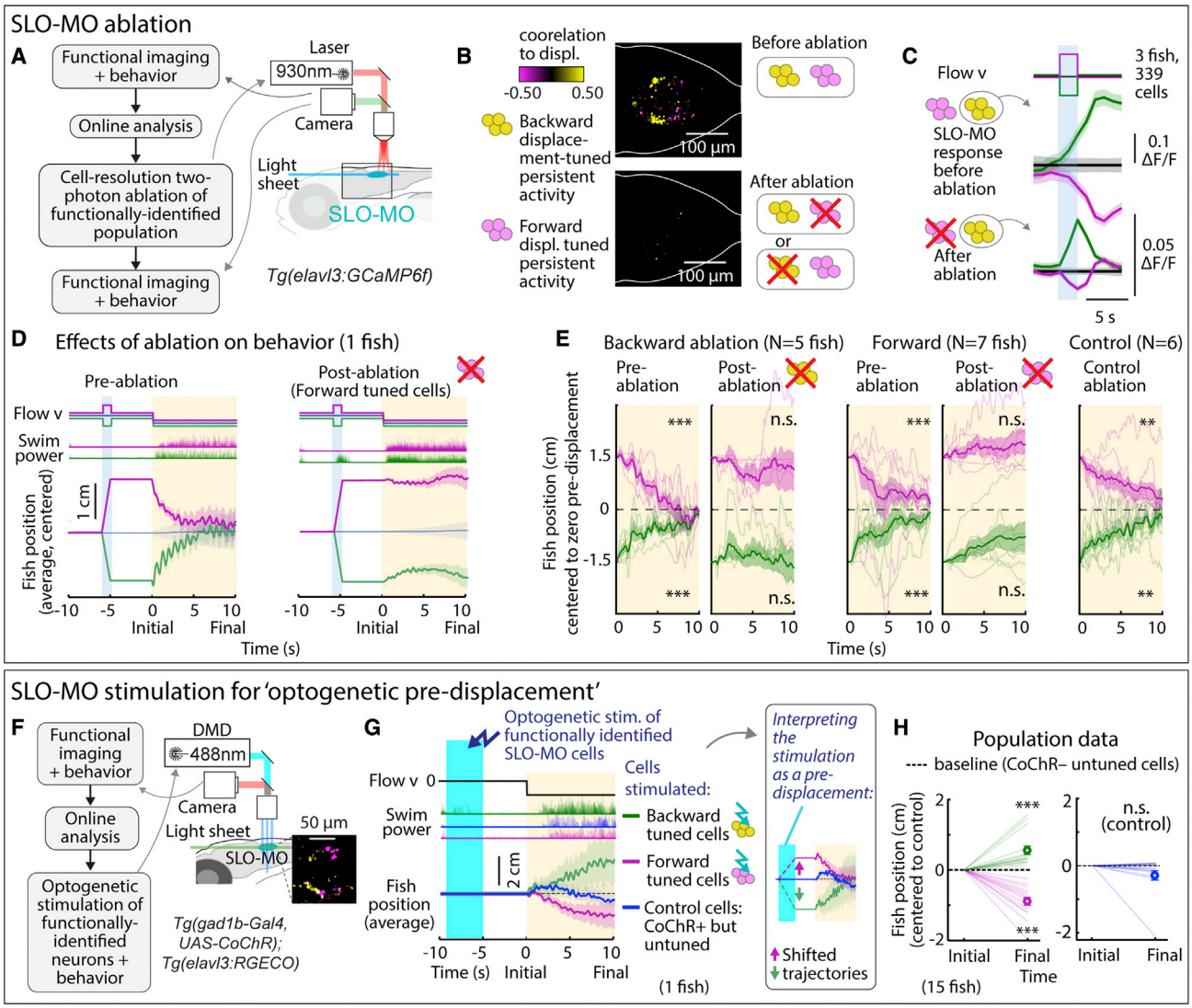

Figure 5. SLO-MO is necessary for location memory and changes future locomotion

(A) Two-photon laser ablation of selected functionally identified SLO-MO neurons in *Tg(elavl3:GCaMP6f)* fish.

(B) Ablating either population (example shown here: ablation of backward pre-displacement tuned cells) abolishes pre-displacement memory capacity of the entire population but leaves short-timescale sensory responses intact (C), suggesting integration through local connectivity within SLO-MO.

(C) Following ablation of one functional population (here, forward displacement tuned neurons), SLO-MO responses of the remaining population (here, backward-tuned neurons) remain visually responsive but lose their persistence. (Shaded regions: SEM in all panels.)

(D) Ablating neurons tuned positively to forward pre-displacement abolishes positional homeostasis in an example fish.

(E) Population data showing consistent abolishment of positional homeostasis across N = 6 fish after ablation of either the forward or the backward pre-displacement encoding population, but not for nearby control neurons. (One-sample t test, ***p < 0.001, p < 2.5e−5 for all pre-ablation, **p < 0.01, p = 3.8e−3 for backward pre-displacements after control ablation, p = 6.4e−2 for forward pre-displacements after control ablation, n.s. p > 0.05. Error bars: SEM in all panels.).

(F) Stimulation setup for activating functionally identified SLO-MO populations using optogenetics in *Tg(gad1b:Gal4; UAS:CoChR; elavl3:jRGECO1b)* fish.

(G) Optogenetic activation of backward pre-displacement encoding neurons (green) causes increased swimming 5–10 s later, and activation of forward pre-displacement encoding neurons (magenta) causes decreased swimming. Control cells that do not encode location do not affect swimming. Inset: manually shifted trajectories to illustrate the similarity to behavior with visual pre-displacements.

(H) Population data showing consistent increases or decreases in swim distance following stimulation of neurons encoding backward or forward pre-displacements. (15 fish, one-sample t test, ***p < 0.001, p = 4.9e−4 for stimulation of backward-tuned SLO-MO cells, p = 2.1e−6 for stimulation of forward-tuned SLO-MO cells, n.s. p > 0.05, p = 0.15 for stimulation of control cells.).

activity in IO neurons and in SLO-MO projections to the IO (Figures 6A and 6B). We identified an anatomical organization of functionally defined SLO-MO projections: SLO-MO activity elicited by backward pre-displacements activated SLO-MO neurites near the medial part of the IO, whereas SLO-MO activity elicited by forward pre-displacements activated SLO-MO

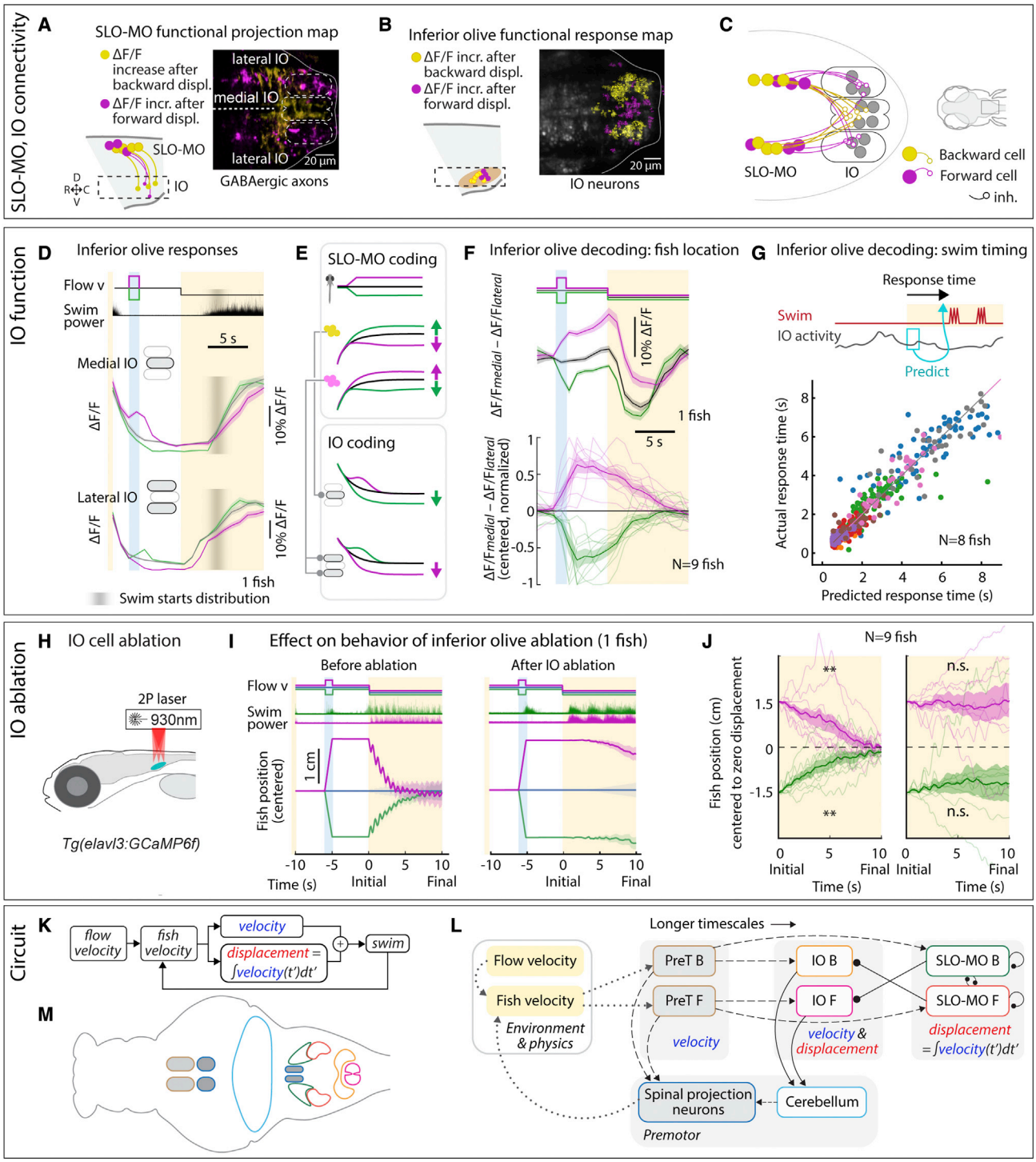

Figure 6. IO is functionally downstream of SLO-MO and necessary for positional homeostasis

(A) Imaging projections from SLO-MO in IO area in *Tg(gad1b:Gal4; UAS:GCaMP6f; elavl3:H2B-jRGECO1b)*. The *gad1b* channel shows anatomical segregation of projections of SLO-MO neurons that encode forward pre-displacements (projections to medial IO) versus backward pre-displacements (projections to lateral IO). Magenta (yellow) stands for forward-pre-displacement-positive (backward-pre-displacement-positive) SLO-MO cells.

(B) Imaging IO neurons (same fish as in A; pan-neuronal channel shown) showing segregation of neurons responding positively to forward pre-displacements (medial IO) versus backward pre-displacements (lateral IO)—the reciprocal of (A), consistent with inhibition of IO by SLO-MO axons. Magenta (yellow) stands for forward displacements (backward displacements) of fish in VR.

(legend continued on next page)

neurites near the lateral IO (Figure 6A). The IO showed complementary responses: medial IO was more active during forward pre-displacements, and lateral IO was more active during backward pre-displacements (Figure 6B), consistent with anatomically organized inhibition of IO neurons by SLO-MO inputs (Figure 6C).

IO activity encoded fish location: backward displacements were followed by persistent decreases in activity in medial IO cells, and forward displacements by decreases in lateral IO activity (Figure 6D). Encoding displacement through decreases in activity suggests these IO neurons have a high baseline firing rate relative to those in mammals.[80] This activity pattern is consistent with a nonlinear response to segregated inhibitory SLO-MO input (Figure 6E). Fish location could thus be decoded from IO activity by taking a weighted difference between medial and lateral activity (Figure 6F). This displacement signal is also a positional error signal in the context of positional homeostasis, where the goal is to minimize displacement. Because the IO is known to project to the cerebellum,[69] a region involved in motor control, we hypothesized that IO activity modulates swimming to implement positional homeostasis.

If IO neurons determine the behavioral response, IO activity should predict properties of future behavior. We constructed a linear predictor of response time from IO responses to forward visual motion before swimming (the first two imaging frames after flow onset). This model accurately predicted variability in response times from variability in IO activity (Figure 6G).[81] Lateral IO was positively correlated with fast responses, whereas medial IO was positively correlated with slow responses (Figure S7M), indicating that SLO-MO-encoded memory suppresses several distinct IO-cerebellum sensorimotor pathways that differentially affect different types of swimming behavior.

To test the causal role of IO in future swimming, we ablated IO neurons at single-cell precision using two-photon laser ablation (Figure 6H). Post-ablation fish were no longer able to perform positional homeostasis (Figures 6I and 6J), although they still responded to the stimulus (e.g., swim traces in Figure 6I). Where intact fish resemble the model fish with memory (Figure 1D, bottom), fish with ablated IO resemble the memoryless model fish (Figure 1D, top). To control for potential damage to SLO-MO caused by the laser being focused near its axons, we inspected SLO-MO activity after IO ablation and found that it still encoded fish location (Figures S7Q and S7R). This result also shows that SLO-MO integration does not require a recurrent feedback loop with the IO. Thus, although the IO is not required for the neural memory trace itself, it is necessary for spatial memory to influence behavior.

We conclude that the control system in Figure 6K is implemented through a neural representation of self-location in the positional integrator SLO-MO that is inherited by the IO. The known role of the IO in error signaling suggests an interpretation of this modulation as a positional error signal. Our working multiregional circuit model underlying positional homeostasis is summarized in Figure 6L (including putative connectivity from the PT to the IO consistent with the control system[40]) and superimposed on the brain in Figure 6M. These results connect self-localization with motor control at the circuit and algorithmic levels.

DISCUSSION

Our results reveal a neural system for self-localization and associated behavior in the vertebrate hindbrain and provide a circuit-level, representational, and control-theoretic understanding of its function. The underlying circuit computes self-location in the dorsal brainstem by integrating optic flow to form a memory of past displacements as the animal actively or passively changes its location. This self-location representation is read out by the IO, analogous to a long-lasting positional error signal[60,69,82–84]—in which the displacement error reflects the difference between the fish's original goal location and its current position. This signal is transformed into locomotor output that corrects for accumulated displacements over tens of seconds or longer. This system functions in a closed-loop with dynamic environments, and the environment-brain-behavior loop encompasses integration, neural representations of self-location, and motor control. The positional integrator of visual self-motion that we identified and named SLO-MO may operate

(C) Hypothesized connectivity between SLO-MO and IO based on (A) and (B).
(D) Time courses of IO responses to location changes. Medial IO is persistently suppressed relative to no pre-displacement following backward pre-displacements. Lateral IO is persistently suppressed relative to no pre-displacement following forward pre-displacements. The initial high ΔF/F levels are carried over from the end of the previous swim period (example fish, population data shown in Figures S7N and S7O).
(E) Schematic of location coding in IO versus SLO-MO and connectivity.
(F) Fish location can be decoded from instantaneous IO activity by taking the difference between medial and lateral IO signals.
(G) Predicting time of first swim bout during the swim period from IO activity at onset of the swim period (before first bout) across 8 fish. Swim time can be predicted, consistent with premotor role of IO.
(H) Schematic of two-photon IO cell ablation.
(I) Example fish positional homeostasis before IO ablation showing intact location memory, and same fish after IO ablation showing a complete loss of location memory.
(J) Population data before and after IO ablation, showing consistent loss of ability to correct for positional shifts after ablation. Animals still swim in response to instantaneous flow, but memory expression is lost. Thus, IO is necessary for self-location memory and accurate positional homeostasis. (9 fish, Wilcoxon sign-rank test, $^{**}p < 0.01$, $p = 7.6e{-}3$.)
(K) Diagram of simplified control system for positional homeostasis, also used to simulate Figure 1D, bottom.
(L) Diagram of hypothesized brain-wide functional circuit. Dotted gray lines: interactions between the brain and environment. Solid black lines: connectivity within the discovered multiregional hindbrain circuit that mediates location memory. Dashed black lines: direct or indirect connections between this circuit and candidate visual and premotor regions. Round head arrows, inhibitory connections; PT, pretectum; IO, inferior olive; SLO-MO, spatial location encoding medulla oblongata neurons. Colors correspond to the annotations in (M).
(M) Approximate anatomical locations of circuit elements diagrammed in (L).

independently and in parallel to circuits in the hippocampal formation, or function as a building block for higher-order representations of self-location in the homologs of the hippocampal formation. Indeed, although this result was not consistent across animals and therefore did not appear in the combined brain maps, in some fish, we observed location-encoding activity in the pallium, which contains the evolutionary predecessor of the hippocampus (Figure S5H). These results demonstrate the need to consider brains at the holistic level and to unify systems neuroscience concepts—such as self-localization and motor control[50,85]—that are often studied separately.

We view the [visual]⇢[SLO-MO]→[IO]→[cerebellum]⇢[premotor] circuit in the context of a brain-wide neural network architecture (Figure 6M). On the visual side, neurons in the PT[35–37,40] known to be responsive to optic flow may directly or indirectly connect to SLO-MO neurons. On the premotor side, the cerebellum may recruit known descending control pathways in the reticulospinal system and caudal hindbrain.[86,87] In the middle, persistence[88] in SLO-MO may be supported by recurrent connectivity, as suggested by the abolishment of persistence following partial ablation of SLO-MO. Connectivity analyses through electron microscopy[89–91] and neuron morphology atlases[92] are likely to clarify these unknowns.

The multiregional circuit described here may have homologs across vertebrates, including mammals. In relation to mouse neuroanatomy,[93] we hypothesize that SLO-MO might overlap with the homolog of the nucleus prepositus hypoglossi (NPH),[94,95] based on GABAergic cell type and functional connectivity to IO,[94,95] as well as location relative to area A2[96] (also known as NE-MO[52]), the nucleus of the solitary tract (NTS), and the fourth ventricle[97] (Figure S7S). Although the NPH has been studied in the context of eye movements,[94,95] it may play a role in navigation by operating in parallel to—or eventually being read out by—hippocampal and entorhinal cortical circuits. This potential homology also raises the possibility that SLO-MO integrates self-location cues and eye movement signals,[87] although no significant correlations to the oculomotor or abducens nuclei were observed in our data. Modern dense electrode arrays[98] may help establish a navigational function for NPH or uncover alternate mappings to homologous circuits in mammalian hindbrain.

Positional homeostasis may be formalized through a ubiquitous element of control theory,[72,99] a PID controller minimizing a displacement error over time. Such a controller implies that locomotion is controlled by a combination of optic flow, its integral, and its derivative. Our results conceptualize SLO-MO as representing the integral term, and the IO as representing a combination of optic flow velocity and its integral (Figures 6K–6M). In particular, Figures 6D–6F shows that IO represents the integral and also responds transiently to velocity. By comparison to the control theoretic description, this IO activity is analogous to the sum of the P term (velocity) and the I term (integrated velocity). Without the integral/SLO-MO, the abstract controller and actual zebrafish become memoryless (Figures 1D top, 5C–5E, and 6H–6J; Figure S7H). This result suggests a hierarchical circuit structure in which a memoryless network mediates the basic OMR response,[36] modulated by olivocerebellar pathways for behavioral flexibility,[72,81,100] which in turn are modulated by SLO-MO pathways that introduce displacement memory. Cerebellar pathways may also be relevant for learned model-based control.[72] These links between SLO-MO and the cerebellum may allow positional homeostasis to be understood through the theoretical frameworks of cerebellum-mediated error signaling and motor control.

Displacement memory is not only useful if fish are passively moved by a current during rest and must correct for this motion later: it is also useful when oscillating water induces back-and-forth displacements that integrate to zero and do not need to be corrected for. More generally, it allows fish to rest and perform other behaviors while also correcting for passive displacements without unnecessary effort (Figure S1A). The SLO-MO to IO projections implement an elegantly simple readout of the displacement memory. SLO-MO's behavioral role likely extends beyond one-dimensional positional homeostasis. For example, a three-dimensional representation of self-displacement and rotation would help zebrafish to effectively navigate in their natural flowing aquatic environment, which could be studied in freely swimming animals.[101,102] SLO-MO may contribute to this ethologically relevant computation, as our data show that sideways virtual displacements of the fish also elicited long-timescale population activity patterns in SLO-MO (Figure 3J), and responses to visual rotations are also observed in the IO.[69] Slow responses to sideways motion are also found in the AHB and PT,[35,37] suggesting these areas may jointly mediate the initial turns in the direction of flow before one-dimensional positional homeostasis is triggered as animals face the flow. Heading representations in the AHB may help maintain the fish's orientation.[19] Cells in this population project to the IPN, the area of which contains position-encoding neurons (Figures 2D, 2G, and S5H), potentially allowing for interactions between motor-driven heading representations and visually driven spatial representations. More generally, effective navigation requires cohesive behavioral strategies that integrate the histories of sensory experience, selected actions, and their behavioral outcomes. The dynamics of SLO-MO neurons likewise reflect an intricate interplay of sensory and motor variables and may be modulated by mechanosensory feedback and vestibular signals.

Our results on location memory and positional homeostasis support the idea that evolutionarily ancient brain regions contribute centrally to higher-order behaviors, which is rapidly gaining empirical support. For example, other elements of cognition, such as evidence accumulation,[35,37,52] heading computation,[19] and behavioral state switching,[52,63,103–105] involve dynamics in unexpected areas of the zebrafish brain, including the hindbrain. Moreover, increasing evidence points to the involvement of unexpected subcortical regions in higher-order mouse behaviors.[106] The idea that cognitive processes are widely distributed across the nervous system aligns with the evolutionary proposition that complex behaviors emerge, in part, by building new circuits on top of ancient brain structures that perform related computations.[107] Brain-wide surveys of neural activity may thus be critical for determining the mechanisms of distributed cognitive function.

Limitations of the study

In our experiments, the zebrafish are paralyzed and swim in a one-dimensional VR environment. A full characterization of the

function of the SLO-MO-IO-cerebellum circuit would benefit from recording and analyzing the circuit in freely swimming fish in three-dimensional flowing aquatic environments.[101,102] Such studies would also address other limitations of the current study by including potential integration of eye movement, vestibular, proprioceptive, and other signals in circuits that might overlap with SLO-MO. It would likewise be interesting to examine how landmarks affect positional homeostasis and neural activity in SLO-MO and find out whether they would enable the animals to truly stabilize their location by eliminating the slow drift in fish position that we observed here. As discussed above, this gradual drift is consistent with a PID control system with leaky positional integration and/or errors in the inference of velocity. Nevertheless, drift might alternatively be due to behavioral motivations occurring in parallel to positional homeostasis, such as exploration,[67,105] in which case positional homeostasis may specifically function to reverse unintended (i.e., not self-generated) position perturbations; more work is needed to evaluate this alternative. Additional work is also needed to identify the connectivity of the multiregional circuit under study to other navigational circuits, including upstream inputs to SLO-MO and potential polysynaptic connections to forebrain structures through electron microscopy connectomics.[89–91] In addition to helping establish homology to mammalian structures, such connectivity analyses, in combination with transcriptomics or proteomics to establish the molecular makeup of SLO-MO cells, would also inform circuit models required for understanding the mechanistic origin of the long timescale integration and possible attractor dynamics in this circuit.

STAR★METHODS

Detailed methods are provided in the online version of this paper and include the following:

ACKNOWLEDGMENTS

This work was supported by the Howard Hughes Medical Institute and by the Simons Foundation (Simons Collaboration on the Global Brain #542943SPI). We thank Albert Lee, Behtash Babadi, Eyal Gruntman, Bradley Hulse, Xinyu Zhao, Ching-Lung Hsu, Sandro Romani, Scott Sternson, David Stern, Vivek Jayaraman, Michael Yartsev, and Florian Engert for discussions and comments on the manuscript; Shin-Ichi Higashijima for help with fish lines; and Minoru Koyama, Paul Tillberg, Greg Fleishman, David Schoppik, Martha Bagnall, Chris De Zeeuw, Robert Baker, David Kleinfeld, and Lauren McElvain for discussions. We thank the GENIE Project Team at Janelia Research Campus for the jGCaMP7 plasmids. We are grateful to the Janelia Research Campus vivarium for support with transgenesis and for fish care, to Marisa Dreher for contributing to figure design, and to Janelia Experimental Technology for help with microscopy.

AUTHOR CONTRIBUTIONS

Conceptualization, E.Y., M.B.A., M.F.Z., J.E.F., and B.D.M.; methodology, E.Y., M.B.A., M.F.Z., M.R., B.J., S.N., N.V., and J.E.F.; investigation, E.Y., M.F.Z., and B.J.; analysis, E.Y., M.B.A., M.F.Z., M.R., B.J., J.E.F., B.D.M., and Z.W.; supervision, M.B.A. and J.E.F.; writing, M.B.A., E.Y., B.D.M., J.E.F., and B.J.

DECLARATION OF INTERESTS

The authors declare no competing interests.

INCLUSION AND DIVERSITY

One or more of the authors of this paper self-identifies as an underrepresented gender minority in their field of research. One or more of the authors of this paper self-identifies as a member of the LGBTQIA+ community. We support inclusive, diverse, and equitable conduct of research.

Received: March 2, 2022
Revised: June 28, 2022
Accepted: November 21, 2022
Published: December 22, 2022

REFERENCES

1. Collett, T.S., and Graham, P. (2004). Animal navigation: path integration, visual landmarks and cognitive maps. Curr. Biol. *14*, R475–R477. https://doi.org/10.1016/j.cub.2004.06.013.
2. Sosa, M., and Giocomo, L.M. (2021). Navigating for reward. Nat. Rev. Neurosci. *22*, 472–487. https://doi.org/10.1038/s41583-021-00479-z.
3. Tolman, E.C. (1948). Cognitive maps in rats and men. Psychol. Rev. *55*, 189–208. https://doi.org/10.1037/h0061626.
4. Behrens, T.E.J., Muller, T.H., Whittington, J.C.R., Mark, S., Baram, A.B., Stachenfeld, K.L., and Kurth-Nelson, Z. (2018). What is a cognitive map? Organizing knowledge for flexible behavior. Neuron *100*, 490–509. https://doi.org/10.1016/j.neuron.2018.10.002.
5. McNaughton, B.L., Battaglia, F.P., Jensen, O., Moser, E.I., and Moser, M.-B. (2006). Path integration and the neural basis of the "cognitive map." Nat. Rev. Neurosci. *7*, 663–678. https://doi.org/10.1038/nrn1932.
6. Moser, E.I., Moser, M.-B., and McNaughton, B.L. (2017). Spatial representation in the hippocampal formation: a history. Nat. Neurosci. *20*, 1448–1464. https://doi.org/10.1038/nn.4653.
7. Whittington, J.C.R., Muller, T.H., Mark, S., Chen, G., Barry, C., Burgess, N., and Behrens, T.E.J. (2020). The Tolman-Eichenbaum machine:

unifying space and relational memory through generalization in the hippocampal formation. Cell *183*, 1249–1263.e23. https://doi.org/10.1016/j.cell.2020.10.024.

8. O'Keefe, J., and Dostrovsky, J. (1971). The hippocampus as a spatial map. Preliminary evidence from unit activity in the freely-moving rat. Brain Res. *34*, 171–175. https://doi.org/10.1016/0006-8993(71)90358-1.
9. Yartsev, M.M., and Ulanovsky, N. (2013). Representation of three-dimensional space in the hippocampus of flying bats. Science *340*, 367–372. https://doi.org/10.1126/science.1235338.
10. Robinson, N.T.M., Descamps, L.A.L., Russell, L.E., Buchholz, M.O., Bicknell, B.A., Antonov, G.K., Lau, J.Y.N., Nutbrown, R., Schmidt-Hieber, C., and Häusser, M. (2020). Targeted Activation of Hippocampal Place Cells Drives Memory-Guided Spatial Behavior. Cell *183*, 2041–2042. https://doi.org/10.1016/j.cell.2020.12.010.
11. Vinepinsky, E., Cohen, L., Perchik, S., Ben-Shahar, O., Donchin, O., and Segev, R. (2020). Representation of edges, head direction, and swimming kinematics in the brain of freely-navigating fish. Sci. Rep. *10*, 14762. https://doi.org/10.1038/s41598-020-71217-1.
12. Broglio, C., Rodríguez, F., Gómez, A., Arias, J.L., and Salas, C. (2010). Selective involvement of the goldfish lateral pallium in spatial memory. Behav. Brain Res. *210*, 191–201. https://doi.org/10.1016/j.bbr.2010.02.031.
13. Ocaña, F.M., Uceda, S., Arias, J.L., Salas, C., and Rodríguez, F. (2017). Dynamics of goldfish subregional hippocampal pallium activity throughout spatial memory formation. Brain Behav. Evol. *90*, 154–170. https://doi.org/10.1159/000478843.
14. Hafting, T., Fyhn, M., Molden, S., Moser, M.-B., and Moser, E.I. (2005). Microstructure of a spatial map in the entorhinal cortex. Nature *436*, 801–806. https://doi.org/10.1038/nature03721.
15. Campbell, M.G., Attinger, A., Ocko, S.A., Ganguli, S., and Giocomo, L.M. (2021). Distance-tuned neurons drive specialized path integration calculations in medial entorhinal cortex. Cell Rep. *36*, 109669. https://doi.org/10.1016/j.celrep.2021.109669.
16. Vann, S.D., Aggleton, J.P., and Maguire, E.A. (2009). What does the retrosplenial cortex do? Nat. Rev. Neurosci. *10*, 792–802. https://doi.org/10.1038/nrn2733.
17. Bassett, J.P., and Taube, J.S. (2001). Neural correlates for angular head velocity in the rat dorsal tegmental nucleus. J. Neurosci. *21*, 5740–5751. https://doi.org/10.1523/JNEUROSCI.21-15-05740.2001.
18. Blair, H.T., Cho, J., and Sharp, P.E. (1998). Role of the lateral mammillary nucleus in the rat head direction circuit: a combined single unit recording and lesion study. Neuron *21*, 1387–1397. https://doi.org/10.1016/s0896-6273(00)80657-1.
19. Petrucco, L., Lavian, H., Wu, Y.K., Svara, F., Štih, V., and Portugues, R. (2022). Neural dynamics and architecture of the heading direction circuit in a vertebrate brain. Preprint at bioRxiv. https://doi.org/10.1101/2022.04.27.489672.
20. Seelig, J.D., and Jayaraman, V. (2015). Neural dynamics for landmark orientation and angular path integration. Nature *521*, 186–191. https://doi.org/10.1038/nature14446.
21. Green, J., Adachi, A., Shah, K.K., Hirokawa, J.D., Magani, P.S., and Maimon, G. (2017). A neural circuit architecture for angular integration in Drosophila. Nature *546*, 101–106. https://doi.org/10.1038/nature22343.
22. Green, J., Vijayan, V., Mussells Pires, P., Adachi, A., and Maimon, G. (2019). A neural heading estimate is compared with an internal goal to guide oriented navigation. Nat. Neurosci. *22*, 1460–1468. https://doi.org/10.1038/s41593-019-0444-x.
23. Collett, M., and Collett, T.S. (2000). How do insects use path integration for their navigation? Biol. Cybern. *83*, 245–259. https://doi.org/10.1007/s004220000168.
24. Chan, E., Baumann, O., Bellgrove, M.A., and Mattingley, J.B. (2012). From objects to landmarks: the function of visual location information in spatial navigation. Front. Psychol. *3*, 304. https://doi.org/10.3389/fpsyg.2012.00304.
25. Boles, L.C., and Lohmann, K.J. (2003). True navigation and magnetic maps in spiny lobsters. Nature *421*, 60–63. https://doi.org/10.1038/nature01226.
26. Fraser, P.J. (2006). Review: depth, navigation and orientation in crabs: angular acceleration, gravity and hydrostatic pressure sensing during path integration. Mar. Freshw. Behav. Physiol. *39*, 87–97. https://doi.org/10.1080/10236240600708439.
27. Jun, J.J., Longtin, A., and Maler, L. (2016). Active sensing associated with spatial learning reveals memory-based attention in an electric fish. J. Neurophysiol. *115*, 2577–2592. https://doi.org/10.1152/jn.00979.2015.
28. Campbell, M.G., Ocko, S.A., Mallory, C.S., Low, I.I.C., Ganguli, S., and Giocomo, L.M. (2018). Principles governing the integration of landmark and self-motion cues in entorhinal cortical codes for navigation. Nat. Neurosci. *21*, 1096–1106. https://doi.org/10.1038/s41593-018-0189-y.
29. Jayakumar, R.P., Madhav, M.S., Savelli, F., Blair, H.T., Cowan, N.J., and Knierim, J.J. (2019). Recalibration of path integration in hippocampal place cells. Nature *566*, 533–537. https://doi.org/10.1038/s41586-019-0939-3.
30. Wehner, R. (2020). Desert Navigator: the Journey of the Ant (Harvard University Press).
31. Mittelstaedt, M.-L., and Mittelstaedt, H. (1980). Homing by path integration in a mammal. Naturwissenschaften *67*, 566–567. https://doi.org/10.1007/BF00450672.
32. Geva-Sagiv, M., Las, L., Yovel, Y., and Ulanovsky, N. (2015). Spatial cognition in bats and rats: from sensory acquisition to multiscale maps and navigation. Nat. Rev. Neurosci. *16*, 94–108. https://doi.org/10.1038/nrn3888.
33. Kim, I.S., and Dickinson, M.H. (2017). Idiothetic path integration in the fruit fly Drosophila melanogaster. Curr. Biol. *27*, 2227–2238.e3. https://doi.org/10.1016/j.cub.2017.06.026.
34. Nakayama, K. (1985). Biological image motion processing: a review. Vision Res. *25*, 625–660. https://doi.org/10.1016/0042-6989(85)90171-3.
35. Dragomir, E.I., Štih, V., and Portugues, R. (2020). Evidence accumulation during a sensorimotor decision task revealed by whole-brain imaging. Nat. Neurosci. *23*, 85–93. https://doi.org/10.1038/s41593-019-0535-8.
36. Naumann, E.A., Fitzgerald, J.E., Dunn, T.W., Rihel, J., Sompolinsky, H., and Engert, F. (2016). From whole-brain data to functional circuit models: the zebrafish optomotor response. Cell *167*, 947–960.e20. https://doi.org/10.1016/j.cell.2016.10.019.
37. Bahl, A., and Engert, F. (2020). Neural circuits for evidence accumulation and decision making in larval zebrafish. Nat. Neurosci. *23*, 94–102. https://doi.org/10.1038/s41593-019-0534-9.
38. Orger, M.B., Smear, M.C., Anstis, S.M., and Baier, H. (2000). Perception of Fourier and non-Fourier motion by larval zebrafish. Nat. Neurosci. *3*, 1128–1133. https://doi.org/10.1038/80649.
39. Srinivasan, M., Zhang, S., Lehrer, M., and Collett, T. (1996). Honeybee navigation en route to the goal: visual flight control and odometry. J. Exp. Biol. *199*, 237–244. https://doi.org/10.1242/jeb.199.1.237.
40. Kramer, A., Wu, Y., Baier, H., and Kubo, F. (2019). Neuronal architecture of a visual center that processes optic flow. Neuron *103*, 118–132.e7. https://doi.org/10.1016/j.neuron.2019.04.018.
41. Major, G., and Tank, D. (2004). Persistent neural activity: prevalence and mechanisms. Curr. Opin. Neurobiol. *14*, 675–684. https://doi.org/10.1016/j.conb.2004.10.017.
42. Widloski, J., and Fiete, I.R. (2014). A model of grid cell development through spatial exploration and spike time-dependent plasticity. Neuron *83*, 989. https://doi.org/10.1016/j.neuron.2014.08.017.
43. Gil, M., Ancau, M., Schlesiger, M.I., Neitz, A., Allen, K., De Marco, R.J., and Monyer, H. (2018). Impaired path integration in mice with disrupted

grid cell firing. Nat. Neurosci. *21*, 81–91. https://doi.org/10.1038/s41593-017-0039-3.

44. Oteiza, P., Odstrcil, I., Lauder, G., Portugues, R., and Engert, F. (2017). A novel mechanism for mechanosensory-based rheotaxis in larval zebrafish. Nature *547*, 445–448. https://doi.org/10.1038/nature23014.
45. Valera, G., Markov, D.A., Bijari, K., Randlett, O., Asgharsharghi, A., Baudoin, J.P., Ascoli, G.A., Portugues, R., and López-Schier, H. (2021). A neuronal blueprint for directional mechanosensation in larval zebrafish. Curr. Biol. *31*, 1463–1475.e6. https://doi.org/10.1016/j.cub.2021.01.045.
46. Orger, M.B., Kampff, A.R., Severi, K.E., Bollmann, J.H., and Engert, F. (2008). Control of visually guided behavior by distinct populations of spinal projection neurons. Nat. Neurosci. *11*, 327–333. https://doi.org/10.1038/nn2048.
47. Neuhauss, S.C., Biehlmaier, O., Seeliger, M.W., Das, T., Kohler, K., Harris, W.A., and Baier, H. (1999). Genetic disorders of vision revealed by a behavioral screen of 400 essential loci in zebrafish. J. Neurosci. *19*, 8603–8615. https://doi.org/10.1523/JNEUROSCI.19-19-08603.1999.
48. Marques, J.C., Lackner, S., Félix, R., and Orger, M.B. (2018). Structure of the zebrafish locomotor repertoire revealed with unsupervised behavioral clustering. Curr. Biol. *28*, 181–195.e5. https://doi.org/10.1016/j.cub.2017.12.002.
49. Johnson, R.E., Linderman, S., Panier, T., Wee, C.L., Song, E., Herrera, K.J., Miller, A., and Engert, F. (2020). Probabilistic models of larval zebrafish behavior reveal structure on many scales. Curr. Biol. *30*, 70–82.e4. https://doi.org/10.1016/j.cub.2019.11.026.
50. Rochefort, C., Arabo, A., André, M., Poucet, B., Save, E., and Rondi-Reig, L. (2011). Cerebellum shapes hippocampal spatial code. Science *334*, 385–389. https://doi.org/10.1126/science.1207403.
51. Ahrens, M.B., Li, J.M., Orger, M.B., Robson, D.N., Schier, A.F., Engert, F., and Portugues, R. (2012). Brain-wide neuronal dynamics during motor adaptation in zebrafish. Nature *485*, 471–477. https://doi.org/10.1038/nature11057.
52. Mu, Y., Bennett, D.V., Rubinov, M., Narayan, S., Yang, C.-T., Tanimoto, M., Mensh, B.D., Looger, L.L., and Ahrens, M.B. (2019). Glia accumulate evidence that actions are futile and suppress unsuccessful behavior. Cell *178*, 27–43.e19. https://doi.org/10.1016/j.cell.2019.05.050.
53. Graf, J. (2016). PID Control Fundamentals (CreateSpace Independent Publishing Platform).
54. Stocker, A.A., and Simoncelli, E.P. (2006). Noise characteristics and prior expectations in human visual speed perception. Nat. Neurosci. *9*, 578–585. https://doi.org/10.1038/nn1669.
55. Müller, M., and Wehner, R. (1988). Path integration in desert ants, Cataglyphis fortis. Proc. Natl. Acad. Sci. USA *85*, 5287–5290. https://doi.org/10.1073/pnas.85.14.5287.
56. Ahrens, M.B., Orger, M.B., Robson, D.N., Li, J.M., and Keller, P.J. (2013). Whole-brain functional imaging at cellular resolution using light-sheet microscopy. Nat. Methods *10*, 413–420. https://doi.org/10.1038/nmeth.2434.
57. Panier, T., Romano, S.A., Olive, R., Pietri, T., Sumbre, G., Candelier, R., and Debrégeas, G. (2013). Fast functional imaging of multiple brain regions in intact zebrafish larvae using selective plane illumination microscopy. Front. Neural Circuits *7*, 65. https://doi.org/10.3389/fncir.2013.00065.
58. Vladimirov, N., Mu, Y., Kawashima, T., Bennett, D.V., Yang, C.T., Looger, L.L., Keller, P.J., Freeman, J., and Ahrens, M.B. (2014). Light-sheet functional imaging in fictively behaving zebrafish. Nat. Methods *11*, 883–884. https://doi.org/10.1038/nmeth.3040.
59. Klapoetke, N.C., Murata, Y., Kim, S.S., Pulver, S.R., Birdsey-Benson, A., Cho, Y.K., Morimoto, T.K., Chuong, A.S., Carpenter, E.J., Tian, Z., et al. (2014). Independent optical excitation of distinct neural populations. Nat. Methods *11*, 338–346. https://doi.org/10.1038/nmeth.2836.
60. De Zeeuw, C.I., Simpson, J.I., Hoogenraad, C.C., Galjart, N., Koekkoek, S.K., and Ruigrok, T.J. (1998). Microcircuitry and function of the inferior olive. Trends Neurosci. *21*, 391–400. https://doi.org/10.1016/s0166-2236(98)01310-1.
61. Randlett, O., Wee, C.L., Naumann, E.A., Nnaemeka, O., Schoppik, D., Fitzgerald, J.E., Portugues, R., Lacoste, A.M.B., Riegler, C., Engert, F., et al. (2015). Whole-brain activity mapping onto a zebrafish brain atlas. Nat. Methods *12*, 1039–1046. https://doi.org/10.1038/nmeth.3581.
62. Bae, Y.-K., Kani, S., Shimizu, T., Tanabe, K., Nojima, H., Kimura, Y., Higashijima, S.-I., and Hibi, M. (2009). Anatomy of zebrafish cerebellum and screen for mutations affecting its development. Dev. Biol. *330*, 406–426. https://doi.org/10.1016/j.ydbio.2009.04.013.
63. Kawashima, T., Zwart, M.F., Yang, C.-T., Mensh, B.D., and Ahrens, M.B. (2016). The serotonergic system tracks the outcomes of actions to mediate short-term motor learning. Cell *167*, 933–946.e20. https://doi.org/10.1016/j.cell.2016.09.055.
64. Kubo, F., Hablitzel, B., Dal Maschio, M., Driever, W., Baier, H., and Arrenberg, A.B. (2014). Functional architecture of an optic flow-responsive area that drives horizontal eye movements in zebrafish. Neuron *81*, 1344–1359. https://doi.org/10.1016/j.neuron.2014.02.043.
65. Wu, Y., Dal Maschio, M., Kubo, F., and Baier, H. (2020). An optical illusion pinpoints an essential circuit node for global motion processing. Neuron *108*, 722–734.e5. https://doi.org/10.1016/j.neuron.2020.08.027.
66. Yildizoglu, T., Riegler, C., Fitzgerald, J.E., and Portugues, R. (2020). A neural representation of naturalistic motion-guided behavior in the zebrafish brain. Curr. Biol. *30*, 2321–2333.e6. https://doi.org/10.1016/j.cub.2020.04.043.
67. Dunn, T.W., Mu, Y., Narayan, S., Randlett, O., Naumann, E.A., Yang, C.T., Schier, A.F., Freeman, J., Engert, F., and Ahrens, M.B. (2016). Brain-wide mapping of neural activity controlling zebrafish exploratory locomotion. eLife *5*, e12741. https://doi.org/10.7554/eLife.12741.
68. Dana, H., Sun, Y., Mohar, B., Hulse, B.K., Kerlin, A.M., Hasseman, J.P., Tsegaye, G., Tsang, A., Wong, A., Patel, R., et al. (2019). High-performance calcium sensors for imaging activity in neuronal populations and microcompartments. Nat. Methods *16*, 649–657. https://doi.org/10.1038/s41592-019-0435-6.
69. Felix, R., Markov, D.A., Renninger, S.L., Tomás, R., Laborde, A., Carey, M.R., et al. (2021). Structural and functional organization of visual responses in the inferior olive of larval zebrafish. Preprint at bioRxiv. https://doi.org/10.1101/2021.11.29.470378.
70. De Zeeuw, C.I., Lisberger, S.G., and Raymond, J.L. (2021). Diversity and dynamism in the cerebellum. Nat. Neurosci. *24*, 160–167. https://doi.org/10.1038/s41593-020-00754-9.
71. Lin, Q., Manley, J., Helmreich, M., Schlumm, F., Li, J.M., Robson, D.N., Engert, F., Schier, A., Nöbauer, T., and Vaziri, A. (2020). Cerebellar neurodynamics predict decision timing and outcome on the single-trial level. Cell *180*, 536–551.e17. https://doi.org/10.1016/j.cell.2019.12.018.
72. Markov, D.A., Petrucco, L., Kist, A.M., and Portugues, R. (2021). A cerebellar internal model calibrates a feedback controller involved in sensorimotor control. Nat. Commun. *12*, 6694. https://doi.org/10.1038/s41467-021-26988-0.
73. Chen, X., Mu, Y., Hu, Y., Kuan, A.T., Nikitchenko, M., Randlett, O., Chen, A.B., Gavornik, J.P., Sompolinsky, H., Engert, F., et al. (2018). Brain-wide organization of neuronal activity and convergent sensorimotor transformations in larval zebrafish. Neuron *100*, 876–890.e5. https://doi.org/10.1016/j.neuron.2018.09.042.
74. Li, N., Daie, K., Svoboda, K., and Druckmann, S. (2016). Robust neuronal dynamics in premotor cortex during motor planning. Nature *532*, 459–464. https://doi.org/10.1038/nature17643.
75. Vladimirov, N., Wang, C., Höckendorf, B., Pujala, A., Tanimoto, M., Mu, Y., Yang, C.-T., Wittenbach, J.D., Freeman, J., Preibisch, S., et al. (2018). Brain-wide circuit interrogation at the cellular level guided by online analysis of neuronal function. Nat. Methods *15*, 1117–1125. https://doi.org/10.1038/s41592-018-0221-x.

76. Cannon, S.C., Robinson, D.A., and Shamma, S. (1983). A proposed neural network for the integrator of the oculomotor system. Biol. Cybern. *49*, 127–136. https://doi.org/10.1007/BF00320393.

77. Seung, H.S. (1996). How the brain keeps the eyes still. Proc. Natl. Acad. Sci. USA *93*, 13339–13344. https://doi.org/10.1073/pnas.93.23.13339.

78. Winograd, M., Destexhe, A., and Sanchez-Vives, M.V. (2008). Hyperpolarization-activated graded persistent activity in the prefrontal cortex. Proc. Natl. Acad. Sci. USA *105*, 7298–7303. https://doi.org/10.1073/pnas.0800360105.

79. Goldman, M.S. (2009). Memory without feedback in a neural network. Neuron *61*, 621–634. https://doi.org/10.1016/j.neuron.2008.12.012.

80. Hong, S., and De Schutter, E. (2008). Purkinje neurons: what is the signal for complex spikes? Curr. Biol. *18*, R969–R971. https://doi.org/10.1016/j.cub.2008.08.056.

81. Bina, L., Romano, V., Hoogland, T.M., Bosman, L.W.J., and De Zeeuw, C.I. (2022). Purkinje cells translate subjective salience into readiness to act and choice performance. Cell Rep. *38*, 110362. https://doi.org/10.1016/j.celrep.2022.110362.

82. Kimpo, R.R., Rinaldi, J.M., Kim, C.K., Payne, H.L., and Raymond, J.L. (2014). Gating of neural error signals during motor learning. eLife *3*, e02076. https://doi.org/10.7554/eLife.02076.

83. Clopath, C., Badura, A., De Zeeuw, C.I., and Brunel, N. (2014). A cerebellar learning model of vestibulo-ocular reflex adaptation in wild-type and mutant mice. J. Neurosci. *34*, 7203–7215. https://doi.org/10.1523/JNEUROSCI.2791-13.2014.

84. Welsh, J.P., Lang, E.J., Suglhara, I., and Llinás, R. (1995). Dynamic organization of motor control within the olivocerebellar system. Nature *374*, 453–457. https://doi.org/10.1038/374453a0.

85. Gao, Z., Davis, C., Thomas, A.M., Economo, M.N., Abrego, A.M., Svoboda, K., De Zeeuw, C.I., and Li, N. (2018). A cortico-cerebellar loop for motor planning. Nature *563*, 113–116. https://doi.org/10.1038/s41586-018-0633-x.

86. Severi, K.E., Böhm, U.L., and Wyart, C. (2018). Investigation of hindbrain activity during active locomotion reveals inhibitory neurons involved in sensorimotor processing. Sci. Rep. *8*, 13615. https://doi.org/10.1038/s41598-018-31968-4.

87. Sun, S., Zuo, Z., Ma, M.M., Qian, C., Chen, L., Zhou, W., Drasbek, K.R., and Zuxiang, L. (2019). Neural circuits mediating visual stabilization during active motion in zebrafish. Preprint at bioRxiv. https://doi.org/10.1101/566760.

88. Miri, A., Daie, K., Arrenberg, A.B., Baier, H., Aksay, E., and Tank, D.W. (2011). Spatial gradients and multidimensional dynamics in a neural integrator circuit. Nat. Neurosci. *14*, 1150–1159. https://doi.org/10.1038/nn.2888.

89. Hildebrand, D.G.C., Cicconet, M., Torres, R.M., Choi, W., Quan, T.M., Moon, J., Wetzel, A.W., Scott Champion, A., Graham, B.J., Randlett, O., et al. (2017). Whole-brain serial-section electron microscopy in larval zebrafish. Nature *545*, 345–349. https://doi.org/10.1038/nature22356.

90. Vishwanathan, A., Ramirez, A.D., Wu, J., Sood, A., Yang, R., Kemnitz, N., Ih, D., Turner, N., Lee, K., Tartavull, I., et al. (2020). Predicting modular functions and neural coding of behavior from a synaptic wiring diagram. Preprint at bioRxiv. https://doi.org/10.1101/2020.10.28.359620.

91. Svara, F., Förster, D., Kubo, F., Januszewski, M., Dal Maschio, M., Schubert, P.J., Kornfeld, J., Wanner, A.A., Laurell, E., Denk, W., et al. (2022). Automated synapse-level reconstruction of neural circuits in the larval zebrafish brain. Nat. Methods *19*, 1357–1366. https://doi.org/10.1038/s41592-022-01621-0.

92. Kunst, M., Laurell, E., Mokayes, N., Kramer, A., Kubo, F., Fernandes, A.M., Förster, D., Dal Maschio, M., and Baier, H. (2019). A cellular-resolution atlas of the larval zebrafish brain. Neuron *103*, 21–38.e5. https://doi.org/10.1016/j.neuron.2019.04.034.

93. Lein, E.S., Hawrylycz, M.J., Ao, N., Ayres, M., Bensinger, A., Bernard, A., Boe, A.F., Boguski, M.S., Brockway, K.S., Byrnes, E.J., et al. (2007). Genome-wide atlas of gene expression in the adult mouse brain. Nature *445*, 168–176. https://doi.org/10.1038/nature05453.

94. Barmack, N.H. (2006). Inferior olive and oculomotor system. Prog. Brain Res. *151*, 269–291. https://doi.org/10.1016/S0079-6123(05)51009-4.

95. De Zeeuw, C.I., Wentzel, P., and Mugnaini, E. (1993). Fine structure of the dorsal cap of the inferior olive and its GABAergic and non-GABAergic input from the nucleus prepositus hypoglossi in rat and rabbit. J. Comp. Neurol. *327*, 63–82. https://doi.org/10.1002/cne.903270106.

96. Rinaman, L. (2011). Hindbrain noradrenergic A2 neurons: diverse roles in autonomic, endocrine, cognitive, and behavioral functions. Am. J. Physiol. Regul. Integr. Comp. Physiol. *300*, R222–R235. https://doi.org/10.1152/ajpregu.00556.2010.

97. Tabor, K.M., Marquart, G.D., Hurt, C., Smith, T.S., Geoca, A.K., Bhandiwad, A.A., Subedi, A., Sinclair, J.L., Rose, H.M., Polys, N.F., et al. (2019). Brain-wide cellular resolution imaging of Cre transgenic zebrafish lines for functional circuit-mapping. eLife *8*, e42687. https://doi.org/10.7554/eLife.42687.

98. Jun, J.J., Steinmetz, N.A., Siegle, J.H., Denman, D.J., Bauza, M., Barbarits, B., Lee, A.K., Anastassiou, C.A., Andrei, A., Aydın, Ç., et al. (2017). Fully integrated silicon probes for high-density recording of neural activity. Nature *551*, 232–236. https://doi.org/10.1038/nature24636.

99. Holman, J.G., Lai, W.W.K., Pichler, P., Saska, D., Lagnado, L., and Buckley, C.L. (2022). Control algorithms underlying the translational optomotor response. Preprint at bioRxiv. https://doi.org/10.1101/2022.03.16.484575.

100. Boyden, E.S., Katoh, A., and Raymond, J.L. (2004). Cerebellum-dependent learning: the role of multiple plasticity mechanisms. Annu. Rev. Neurosci. *27*, 581–609. https://doi.org/10.1146/annurev.neuro.27.070203.144238.

101. Cong, L., Wang, Z., Chai, Y., Hang, W., Shang, C., Yang, W., Bai, L., Du, J., Wang, K., and Wen, Q. (2017). Rapid whole brain imaging of neural activity in freely behaving larval zebrafish (Danio rerio). eLife *6*, e28158. https://doi.org/10.7554/eLife.28158.

102. Kim, D.H., Kim, J., Marques, J.C., Grama, A., Hildebrand, D.G.C., Gu, W., Li, J.M., and Robson, D.N. (2017). Pan-neuronal calcium imaging with cellular resolution in freely swimming zebrafish. Nat. Methods *14*, 1107–1114. https://doi.org/10.1038/nmeth.4429.

103. Lovett-Barron, M., Andalman, A.S., Allen, W.E., Vesuna, S., Kauvar, I., Burns, V.M., and Deisseroth, K. (2017). Ancestral circuits for the coordinated modulation of brain state. Cell *171*, 1411–1423.e17. https://doi.org/10.1016/j.cell.2017.10.021.

104. Lovett-Barron, M., Chen, R., Bradbury, S., Andalman, A.S., Wagle, M., Guo, S., and Deisseroth, K. (2020). Multiple convergent hypothalamus—brainstem circuits drive defensive behavior. Nat. Neurosci. *23*, 959–967.

105. Marques, J.C., Li, M., Schaak, D., Robson, D.N., and Li, J.M. (2020). Internal state dynamics shape brainwide activity and foraging behaviour. Nature *577*, 239–243. https://doi.org/10.1038/s41586-019-1858-z.

106. Steinmetz, N.A., Zatka-Haas, P., Carandini, M., and Harris, K.D. (2019). Distributed coding of choice, action and engagement across the mouse brain. Nature *576*, 266–273. https://doi.org/10.1038/s41586-019-1787-x.

107. Striedter, G.F., and Glenn Northcutt, R. (2019). Brains Through Time: A Natural History of Vertebrates (Oxford University Press).

108. Dana, H., Mohar, B., Sun, Y., Narayan, S., Gordus, A., Hasseman, J.P., Tsegaye, G., Holt, G.T., Hu, A., Walpita, D., et al. (2016). Sensitive red protein calcium indicators for imaging neural activity. eLife *5*, e12727. https://doi.org/10.7554/eLife.12727.

109. Freeman, J., Vladimirov, N., Kawashima, T., Mu, Y., Sofroniew, N.J., Bennett, D.V., Rosen, J., Yang, C.-T., Looger, L.L., and Ahrens, M.B. (2014). Mapping brain activity at scale with cluster computing. Nat. Methods *11*, 941–950. https://doi.org/10.1038/nmeth.3041.

110. Westerfield, M. (2000). A Guide for the Laboratory Use of Zebrafish (Danio rerio), Fourth Edition (University of Oregon Press).

111. Uchida, D., Yamashita, M., Kitano, T., and Iguchi, T. (2002). Oocyte apoptosis during the transition from ovary-like tissue to testes during sex differentiation of juvenile zebrafish. J. Exp. Biol. *205*, 711–718. https://doi.org/10.1242/jeb.205.6.711.

112. White, R.M., Sessa, A., Burke, C., Bowman, T., LeBlanc, J., Ceol, C., Bourque, C., Dovey, M., Goessling, W., Burns, C.E., et al. (2008). Transparent adult zebrafish as a tool for in vivo transplantation analysis. Cell Stem Cell *2*, 183–189. https://doi.org/10.1016/j.stem.2007.11.002.

113. Satou, C., Kimura, Y., and Higashijima, S.-I. (2012). Generation of multiple classes of V0 neurons in zebrafish spinal cord: progenitor heterogeneity and temporal control of neuronal diversity. J. Neurosci. *32*, 1771–1783. https://doi.org/10.1523/JNEUROSCI.5500-11.2012.

114. Satou, C., Kimura, Y., Hirata, H., Suster, M.L., Kawakami, K., and Higashijima, S.-I. (2013). Transgenic tools to characterize neuronal properties of discrete populations of zebrafish neurons. Development *140*, 3927–3931. https://doi.org/10.1242/dev.099531.

115. Urasaki, A., Asakawa, K., and Kawakami, K. (2008). Efficient transposition of the Tol2 transposable element from a single-copy donor in zebrafish. Proc. Natl. Acad. Sci. USA *105*, 19827–19832. https://doi.org/10.1073/pnas.0810380105.

116. Kler, S., Ma, M., Narayan, S., Ahrens, M.B., and Pan, Y.A. (2021). Cre-dependent anterograde transsynaptic labeling and functional imaging in zebrafish using VSV with reduced cytotoxicity. Front. Neuroanat. *15*, 758350. https://doi.org/10.3389/fnana.2021.758350.

117. Fang-Yen, C., Gabel, C.V., Samuel, A.D.T., Bargmann, C.I., and Avery, L. (2012). Laser microsurgery in Caenorhabditis elegans. Methods Cell Biol. *107*, 177–206. https://doi.org/10.1016/B978-0-12-394620-1.00006-0.

118. Vogel, A., and Venugopalan, V. (2003). Mechanisms of pulsed laser ablation of biological tissues. Chem. Rev. *103*, 577–644. https://doi.org/10.1021/cr010379n.

119. Miri, A., Daie, K., Burdine, R.D., Aksay, E., and Tank, D.W. (2011). Regression-based identification of behavior-encoding neurons during large-scale optical imaging of neural activity at cellular resolution. J. Neurophysiol. *105*, 964–980. https://doi.org/10.1152/jn.00702.2010.

120. Avants, B.B., Yushkevich, P., Pluta, J., Minkoff, D., Korczykowski, M., Detre, J., and Gee, J.C. (2010). The optimal template effect in hippocampus studies of diseased populations. Neuroimage *49*, 2457–2466. https://doi.org/10.1016/j.neuroimage.2009.09.062.

121. Berry, M.W., Browne, M., Langville, A.N., Pauca, V.P., and Plemmons, R.J. (2007). Algorithms and applications for approximate nonnegative matrix factorization. Comput. Stat. Data Anal. *52*, 155–173. https://doi.org/10.1016/j.csda.2006.11.006.

122. Hoyer, P.O. (2004). Non-negative matrix factorization with sparseness constraints. J. Mach. Learn. Res. *5*, 1457–1469.

123. Zhu, P., Fajardo, O., Shum, J., Zhang Schärer, Y.-P., and Friedrich, R.W. (2012). High-resolution optical control of spatiotemporal neuronal activity patterns in zebrafish using a digital micromirror device. Nat. Protoc. *7*, 1410–1425. https://doi.org/10.1038/nprot.2012.072.

124. Mensh, B.D., Aksay, E., Lee, D.D., Seung, H.S., and Tank, D.W. (2004). Spontaneous eye movements in goldfish: oculomotor integrator performance, plasticity, and dependence on visual feedback. Vision Res. *44*, 711–726. https://doi.org/10.1016/j.visres.2003.10.015.

125. Aksay, E., Olasagasti, I., Mensh, B.D., Baker, R., Goldman, M.S., and Tank, D.W. (2007). Functional dissection of circuitry in a neural integrator. Nat. Neurosci. *10*, 494–504. https://doi.org/10.1038/nn1877.

126. Miri, A., Bhasin, B.J., Aksay, E.R.F., Tank, D.W., and Goldman, M.S. (2022). Oculomotor plant and neural dynamics suggest gaze control requires integration on distributed timescales. Preprint at bioRxiv. https://doi.org/10.1101/2021.06.30.450653.

STAR★METHODS

KEY RESOURCES TABLE

REAGENT or RESOURCE	SOURCE	IDENTIFIER
Chemicals, peptides, and recombinant proteins		
Alpha-Bungarotoxin	Sigma-Aldrich	Cat# B137
Experimental models: Organisms/strains		
Tg(elavl3:GCaMP6f)^{jf1}	Janelia Research Campus (JRC)[67]	N/A
Tg(elavl3:jGCaMP7f)^{jf96}	JRC (this paper)	N/A
Tg(elavl3:H2B-GCaMP6f)^{jf7}	JRC[67]	N/A
Tg(elavl3:H2B-jGCaMP7f)^{jf90}	JRC (this paper)	N/A
Tg(elavl3:jRGECO1b)^{jf17}	JRC[108]	N/A
Tg(Gad1b:Gal4)^{jf49}*;Tg(UAS:GCaMP6f)*^{jf46}	JRC[52]	N/A
Tg(Gad1b:Gal4)^{jf49}*;Tg(UAS:jGCaMP6f)*^{jf46}*; Tg(elavl3:H2B-jRGECO1a)*^{jf112}	JRC (this paper)	N/A
Tg(gad1b:Gal4)^{jf49}*; Tg(UAS: CoChR-eGFP)*^{jf44}	JRC[52]	N/A
Tg(gad1b:Gal4)^{jf49}*;Tg(UAS:CoChR-eGFP)*^{jf44}*; Tg(elavl3:H2B-jRGECO1a)*^{jf112}	JRC (this paper)	N/A
Tg(elavl3:ReaChR-TagRFP-T)^{jf10}	JRC[67]	N/A
Software and algorithms		
MATLAB	MathWorks	https://www.mathworks.com
ImageJ	National Institutes of Health	https://imagej.nih.gov/ij/
C# (.NET Framework 3.5) (stimulus/behavior)	Microsoft	https://docs.microsoft.com/en-us/dotnet/csharp/
Cell segmentation and component detection	This paper	https://github.com/mikarubi/voluseg, https://doi.org/10.5281/zenodo.7341100
Python 3	Python	https://www.python.org/
Motion correction and fast linear regression	Freeman et al.[109]	https://github.com/nvladimus/ZebrafishFunctionalMaps_LinearRegression, https://doi.org/10.5281/zenodo.7341070
Thunder package	Freeman et al.[109]	https://doi.org/10.1038/nmeth.3041

RESOURCE AVAILABILITY

Lead contact

Further information and requests for resources and reagents should be directed to the corresponding author Misha B. Ahrens (ahrensm@janelia.hhmi.org).

Materials availability

Transgenic zebrafish will be deposited on ZIRC or made available directly to requesting laboratories.

Data and code availability

- Imaging and behavioral data reported in this study are available upon request.
- The python code of the data processing pipeline is available at (https://github.com/nvladimus/ZebrafishFunctionalMaps_LinearRegression) and uses the Thunder package which can be downloaded at http://thunder-project.org. The volumetric segmentation pipeline is available at https://github.com/mikarubi/voluseg.
- Any additional information required to reanalyze the data reported is available from the lead contact upon request.

EXPERIMENTAL MODEL AND SUBJECT DETAILS

Zebrafish

All experiments presented in this study were conducted according to the animal research guidelines from NIH and were approved by the Institutional Animal Care and Use Committee and Institutional Biosafety Committee of Janelia Research Campus. All larvae were reared at 14:10 light-dark cycles according to standard protocols at 28.5C.[110] Zebrafish from 5 to 7 dpf were fed rotifers and used for experiments. Zebrafish sex cannot be determined until ~3 weeks post-fertilization,[111] so experimental animals' sex was unknown.

Transgenesis

Transgenic zebrafish larvae were in casper or nacre background.[112] The fish lines *TgBAC(glyt2:loxP-DsRed-loxP-GFP)*, Satou et al.,[113] *TgBAC(slc17a6b:loxP-DsRed-loxP-GFP)*, Satou et al.[114] and *Tg(gad1b:loxP-RFP-loxP-Gal4)^{jf99}* were all used without Cre-mediated recombination and referred to as *Tg(glyt2:dsRed)*, *Tg(vGlut2a:dsRed)* and *Tg(gad1b:dsRed)* respectively.

The fish lines *Tg(elavl3:GCaMP6f)^{jf1}*, *Tg(elavl3:H2B-GCaMP6f)^{jf7}*, *Tg(elavl3:ReaChR-TagRFP-T)^{jf10}*, and *Tg(elavl3:jRGECO1b)^{jf17}* are described in Dunn et al.,[67] Vladimirov et al.,[75] and Dana et al.[108] *Tg(Gad1b:Gal4)^{jf49}*, *(UAS:GCaMP6f)^{jf46}* and *Tg(gad1b:Gal4)^{jf49}*, *(UAS:CoChR-eGFP)^{jf44}* are described in Mu et al.[52]

Tg(elavl3:jGCaMP7f)^{jf96}, *Tg(elavl3:H2B-jGCaMP7f)^{jf90}*, *Tg(elavl3:H2B-jRGECO1a)^{jf112}* lines were generated with the Tol2 system[115] and published jGCaMP7f and jRGECO1a constructs.[68,108]

For imaging of neural activity we used transgenic zebrafish lines expressing:

- Cytosolic GCaMP6f, *Tg(elavl3:GCaMP6f)^{jf1}* (Dunn et al.[67])
- Cytosolic jGCaMP7f, *Tg(elavl3:jGCaMP7f)^{jf96}* (this paper)
- Nuclear-localized GCaMP6f, *Tg(elavl3:H2B-GCaMP6f)^{jf7}* (Dunn et al.[67])
- Nuclear-localized jGCaMP7f, *Tg(elavl3:H2B-jGCaMP7f)^{jf90}* (this paper)
- Cytosolic jRGECO, *Tg(elavl3:jRGECO1b)^{jf17}* (Dana et al.[108])
- *Tg(Gad1b:Gal4)^{jf49};Tg(UAS:GCaMP6f)^{jf46}* (Mu et al.[52])
- *Tg(Gad1b:Gal4)^{jf49};Tg(UAS:jGCaMP6f)^{jf46};Tg(elavl3:H2B-jRGECO1a)^{jf112}* (this paper)

For neurotransmitter identity determination we used:

- *Tg(vGlut2a:dsRed)* - (*TgBAC(slc17a6b:loxP-DsRed-loxP-GFP)*, Satou et al.[114])
- *Tg(glyt2:dsRed)* - (*TgBAC(glyt2:loxP-DsRed-loxP-GFP)*, Satou et al.[113])
- *Tg(gad1b:dsRed)* - (*Tg(gad1b:loxP-RFP-loxP-Gal4)^{jf99}*) (Kler et al.[116])

For optogenetic stimulations we used:

- *Tg(gad1b:Gal4)^{jf49}*; *Tg(UAS:CoChR-eGFP)^{jf44}* (Mu et al.[52])
- *Tg(gad1b:Gal4)^{jf49}*; *Tg(UAS:CoChR-eGFP)^{jf44}*; *Tg(elavl3:H2B-jRGECO1a)^{jf112}* (this paper)
- *Tg(elavl3:ReaChR-TagRFP-T)^{jf10}* (Dunn et al.[67])

METHOD DETAILS

Light-sheet microscopy

The design of our light-sheet microscope and behavior setup is as described earlier.[58,75] Briefly, the detection arm consisted of a water-dipping detection objective (16x/0.8 NA, Nikon) mounted vertically on a piezo stage (Physik Instrumente), a tube lens and an sCMOS camera (Orca Flash 4.0, Hamamatsu). The detection arm was equipped with a band-pass filter (525/50 nm, Semrock) and long-pass filter (590 nm, Semrock) for separating GCaMP and RGECO fluorescence light from scattered 488 nm and 561 nm laser light, respectively. Each of the two illumination arms consisted of an air illumination objective (4x/0.28 NA, Olympus) mounted horizontally on a piezo stage, a tube lens, an f-theta lens and a pair of galvanometer scanners (Cambridge Technology). The scan mirrors and f-theta lens scanned the collimated laser beam (488 nm / 561 nm) laterally and along the z-axis of the image space. The excitation laser was rapidly turned off electronically every time the laser was scanned over the eye of the fish to avoid direct stimulation of the retina.

Preparation of zebrafish for fictive behavior and imaging experiments

All animal handling procedures were done as previously described.[63,75] Larval zebrafish at 6–7 dpf were paralyzed by immersion in 1 mg/ml alpha-bungarotoxin solution (Invitrogen) dissolved in external solution (in mM: 134 NaCl, 2.9 KCl, 2.1 $CaCl_2$, 1.2 $MgCl_2$, 10 HEPES, 10 glucose [pH 7.8]; 290 mOsm). Duration of immersion was empirically determined, ranging from 20 to 40 seconds. Once paralyzed, the fish were embedded using 2% low-melting point agarose (Sigma-Aldrich Inc.) in a custom made chamber (designs available upon request), with agarose removed from the animal to expose the tail (for electrophysiological recordings[51]) and head

(for imaging). Extracellular recordings from the tail were made with borosillicate pipettes (TW150-3, World Precision Instruments) pulled by a vertical puller (PC-10, Narishige) and shaped by a microforge (MF-900, Narishige) to have a tip diameter of approximately 40 micrometers. Recordings were made using an Axon Multiclamp 700B amplifier in current clamp and acquired using National Instruments DAQ boards. Signals were sampled at 6 kHz, and band-pass filtered with a 3 kHz/100 Hz low-pass/high-pass cutoff.

Behavioral assays and visual stimulus delivery

To identify swim bouts, signals were further processed by taking the local standard deviation in a sliding 10 ms window, after which a simple thresholding operation was used to identify swims. Signals were recorded and visual stimuli presented using custom software written in C# (Microsoft). A diffusive plastic screen was attached to the bottom of the chamber from the outside, ~1 cm below the fish, to allow image projections from below using a miniature projector (Sony Pico Mobile Projector; MP-CL1) connected to the behavior acquisition and control computer.

Experiments were performed in 1D virtual environments consisting either of finely spaced (~2 mm thickness) red/black bars or irregular random red/black patterns to image GCaMP fish; green/black gratings or patterns were used when imaging jRGECO1b fish. Irregular patterns (Figures 1A and 1B) were generated by creating a 2D Gaussian random phase noise and weighting it in Fourier space with a weighting function proportional to $1/(freq_x + freq_y)$, inverse Fourier transforming it, scaling it to lie between 0 and 1, and thresholding it at 0.32 and 0.68 to create noise patterns as in Figure 1B. These visual stimuli formed the patterns of a virtual track through which fish swam, with periods of backward, stationary, and forward motion as described in Figure 1C and other figures detailing the behavioral assays. Bout power was defined as the integrated windowed standard deviation of the electrical signal from the tail recording as in Dunn et al.[67]

Imaging of neural activity

Whole brain imaging using light-sheet microscopy as in Figure 2 was performed using both lateral and frontal light-sheet illumination arms on volumes spanning 300 μm along the dorso-ventral axis (61 z-planes, 5 μm intervals) and ~800 and ~500 μm along the longitudinal and lateral axes in *Tg(elavl3:jGCaMP7f)*^{jf1} fish; imaging of the hindbrain in Figures 3, 4, 5, and 6 was performed using only the lateral illumination arm on volumes with variable dimensions spanning the regions of interest, ranging from 400 to 600 μm along the longitudinal axis. High-speed calcium imaging of SLO-MO neurons in Figure S6K was performed using *Tg(Gad1b:Gal4; UAS:GCaMP6f)* by imaging a single plane around the SLO-MO cluster at 33 Hz in the light sheet microscope. High-speed calcium imaging of IO neurons in Figures 6A, 6B, 6G, and S7M, was performed using *Tg(Gad1b:Gal4)*^{jf49}*; Tg(UAS:jGCaMP6f)*^{jf46}; *Tg (elavl3:H2B-jRGECO1a)*^{jf112} by imaging 9 planes (45 μm thick in total) around IO clusters.

Neuron ablations

To ablate individual neurons we used two-photon laser plasma ablation based on published protocols and optimized to act on sub-single-neuron spatial scales.[117,118] We used high power laser (500 mW, measured after the objective) at 930 nm wavelength with a short exposure time (1-2 ms for neurons 0-100 μm from the dorsal brain surface and up to 3-4 ms in ventral areas 150-200 μm deep) using a Coherent Chameleon Ultra II laser. The time interval between successive ablation points was set to 5 seconds to allow heat and chemicals released by cell ablation to dissipate and minimize unintended brain damage.

In the behavioral tests, the optomotor (OMR) assay was started 20 minutes before ablation, followed by an ablation session lasting 5-10 minutes, followed by further OMR behavior trials for another 30-40 minutes after ablation. Ablation of SLO-MO neurons was performed by first analyzing neural activity on a computer cluster to generate functional brain maps, then selecting specific sets of functionally-defined neurons for two-photon laser ablation at single-cell resolution (Figure 5A) using the techniques described in Vladimirov et al.[75] Ablation of IO neurons was based on known anatomy and did not require prior functional analysis. Ablation results are shown in Figures 5A–5E, 6H–6J, S7A–S7H, and S7P–S7R.

Optogenetics

For the function-guided optogenetic stimulation of SLO-MO neurons (Figures 2K, 2M, 5F–5H, and S7I–S7L) we used a similar approach for identifying SLO-MO neurons[75] during the experiment, then used a digital micromirror device (DMD)-based (LightCrafter Discovery Kit, Texas Instruments) method to deliver 488 nm light pulses to predefined Regions Of Interest (ROIs) with approximately single-cell precision (for more details, see Mu et al.[52]). Fish of genotype *Tg(gad1b:Gal4)*^{jf49}*; Tg(UAS:CoChR-eGFP)*^{jf44}*; Tg(elavl3:H2B-jRGECO1a)*^{jf112} at 6 d.p.f. were imaged using a 561 nm excitation laser in a 10-minute experiment in which swimming was induced by alternating 10-second periods of no movement and backward movement through VR with a brief pre-displacement inserted during the no-movement period, as described in Figure 1. SLO-MO neurons were identified using pixel-wise Spearman correlation after cross-correlation based registration,[109,119] with maps cross-referenced to those showing CoChR expression patterns in each fish. In each experiment, 5 to 14 CoChR-expressing SLO-MO neurons were selected for subsequent stimulation (3-7 per condition), with the same number of nearby non-SLO-MO CoChR-expressing cells and an area outside the brain selected as controls.

For Figures 2K, 2M, S7K, and S7L, after SLO-MO cells were identified, the fish chamber was placed in the dark. The following experiments were performed without providing any visual stimulus. The 488 nm stimulation laser was pulsed at 10 Hz with 60 ms pulses during whole-hindbrain imaging. Each ROI was stimulated for 2.5 s, 3.5 s, 5 s or 10 s. Experiments lasted at least 60 minutes

depending on the number of ROIs. Stimulation epochs were interspersed by rest periods of 40 s. In order to identify functional connectivity unambiguously, we stimulated all identified SLO-MO cells, but individually, one cell at a time, each SLO-MO cell making up one ROI. We then combined the resulting inhibition maps from all SLO-MO cells across fish, shown in Figure 2M. Since we stimulated one cell at a time, we did not expect significant memory effects, although stimulating some individual SLO-MO cells for 3.5 s did give rise to long-lasting persistent activity (10 s to 12 s). To calculate Figure S7L, for each stimulation location (ROI), we took the largest inhibition it caused in the IO, then averaged it across all cells within a brain area or all control cells, across fish.

For Figures 5F–5H, S7I, and S7J, the same setup and DMD stimulation paradigm (10 Hz, 60 ms pulses) were used. After SLO-MO cells are identified, a behavioral paradigm consisting of 10 s delay period alternating with 10 s swim period (as described in the main text) was used to induce behavior. All identified backward tuned SLO-MO cells were stimulated at the same time, or all forward tuned SLO-MO cells were stimulated at the same time, or control cells were stimulated. Stimulation epochs were interspersed by rest periods of 40 s.

Extraction of cells from voxel data

We extracted populations of cell bodies and sections of neuropil ('cell segments') from raw fluorescence data with a volumetric segmentation pipeline first described in Mu et al.[52] and available from https://github.com/mikarubi/voluseg. We first registered all volumes to the volume recorded halfway through the experiment using ANTs.[120] We then defined an intensity-based brain mask and divided the masked volume into about 2000 spatially contiguous and slightly overlapping volumetric blocks. A block typically contained about 100 tightly packed 5 μm diameter cell spheres.

We initialized the spatial footprint of each cell as a local-intensity peak of strongly correlated and contiguous voxels. We then used constrained non-negative matrix factorization to segment each block in parallel. For n voxels, t timepoints, and c cell segments we factorized,

$$V_{n\times t} \approx W_{n\times c} H_{c\times t} + X_{n\times 1} I_{1\times t} \quad \text{(Equation 1)}$$

where V is the full spatiotemporal fluorescence matrix for each block W and H are, respectively, the spatial footprint and temporal trace of cell segments, and X and I are the corresponding spatial footprint and temporal trace of the background signal.

We solved Equation 1 approximately using alternating least-squares.[121] We regularized the spatial cell footprint W by restricting it to a contiguous segment within a 10 μm diameter sphere, and by projecting to a sparse subspace.[122] We compute the baseline of the resulting fluorescence with a sliding-window percentile filter that estimated the 10th percentile of the data in the units reported by the camera in 5-minute windows (i.e. this estimate of F_{baseline} includes $F_{\text{background}}$ which must be subtracted in the denominator). We then computed $\Delta F/F$ as:

$$\Delta F \Big/ F = \frac{F_{\text{raw}} - F_{\text{baseline}}}{F_{\text{baseline}} - F_{\text{background}}}$$

Registration of brains onto a reference brain

To compare results across analyses we registered all experiments to a representative brain volume, using iterative rigid-body, affine, and diffeomorphic non-rigid image registration, implemented in ANTs.[120]

Computation of the brain activity maps

We computed the functional maps from the time-varying GCaMP6f and jGCAMP7f intensity signal in segmented cells using the methods described above. The time series of all cells segmented in the brain (segmented neurons) were first separated into multiple individual trials. Specifically, an activity array was constructed containing the $\Delta F/F$ information, but organized to have size [l(number of neurons segmented)×m(number of trials)×t(number of time points in each trial)]. Another array containing information on presented stimuli (such as past location displacement) or behavioral aspects (such as current fish body location) of the matching trials was constructed, of size [m(number of trials)×t(number of time points in each trial)]. A Spearman correlation between the two matrices was computed for all individual cells at each time point across trials, resulting in a correlation coefficient matrix and a corresponding p-value matrix.

Figure 2D was computed using the trial structure presented in Figure 1E, with a 5-second delay period after the pre-displacements and a 10-second swim period. To locate neurons encoding self-location during the entire trial including both the 5 second delay period after pre-displacement and the 10 second swim period, the Spearman correlation was computed for every neuron in the brain between its [$m\times t$] $\Delta F/F$ matrix and an [$m\times t$] matrix of current fish location (where m is the number of trials, and t is the number of time points in each trial). A correlation coefficient array of length t was then computed for each individual segmented neuron, as well as its p-value. In this map (Figure 2D), only neurons with persistent correlation to its current self-location are included. The selection criteria is that for all time points after position displacement, at least 80% of all time points (12 seconds out of 15 seconds) must satisfy $p<0.005$. The correlation coefficient for each cell shown in the heat map is the average correlation coefficient of that cell for all the time points considered. This process was repeated for each individual fish, and all cells meeting these criteria were extracted and used for subsequent analysis.

Figure 2E was computed from the trial structure presented in Figure 2C, containing a long delay period (17 seconds) after the pre-displacements to locate long time constant position displacement memory cells. The Spearman correlation was computed for every neuron in the brain between a [$m \times t$] matrix of $\Delta F/F$ and a [$m \times t$] matrix of pre-displacement data, then a correlation coefficient array with length t was computed for each individual neuron, as well as its p-value. In this map, only neurons with persistent correlation to the pre-displacement ($p<0.005$ during the entire last 10 seconds before the subsequent swim period, which is from 7 seconds to 17 seconds) are included. The correlation coefficient for each cell shown in the heat map is the average correlation coefficient of the 10 s considered for that cell. This process was repeated for each individual fish, and all cells meeting these criteria were extracted and used for subsequent analysis.

Figure 2F was computed from all fish from the trial structure presented in Figure 1E, focusing on the response of neurons at the start of the *swim* period before the fish starts to swim to locate cells predicting future swim distance. A $\Delta F/F$ array of size [l(number of neurons)$\times m$(number of trials)$\times$2(first two time points after swim period onset before fish swims)] was constructed. Another array of size [m(number of trials)$\times$2] containing information of the swim distance in the swim period of the current trial was constructed. The Spearman correlation was then computed for every neuron in the brain between an [$m \times 2$] matrix of $\Delta F/F$ and an [$m \times 2$] matrix of future swim distances. (The purpose of duplication of swim distance here ($\times$2) is to match dimensionalities of that of the $\Delta F/F$ array.) A correlation coefficient array with length 2 was then computed for each individual neuron, as well as its p-value. In this map, only neurons with $p<0.005$ for both time points were included. This process was repeated for each individual fish, and all cells meeting these criteria were extracted and used for subsequent analysis.

To combine data across fish, the maps obtained above from individual fish were processed across fish via a statistical test described in Marques et al.[105] to produce the final maps shown in Figures 2D–2F. This statistical test ascribes a p-value to each neuron based on the distribution of similar functionally-defined neurons in other fish. This p-value was used to discard neurons that had no consistent nearby partners in other fish: only neurons with $p<0.001$ were kept. In this shuffle test, the null hypothesis is that the average minimal distance of each neuron in each individual fish to neurons of the same functional class in other fish is the same as its minimal distance to a random neuron (5000 times shuffle repetition) in other fish.

In Figure 2H, the number of neurons that can predict future swim distance was calculated from Figure 2F; while the neurons that have pre-displacement memory were defined as neurons that encode pre-displacement for longer than 5 seconds. Note that memory-encoding cells in Figure 2E encode the pre-displacement for at least 17 seconds.

Hybrid anatomical-functional tracing of SLO-MO neurites

In Figure 2J, a time course for each functionally identified SLO-MO cell body was computed, then the $\Delta F/F$ time series of each voxel in the volume was correlated to the cell body $\Delta F/F$ time series. The grayscale in the figure is the maximal correlation for each voxel to a SLO-MO cell body. The resulting volume is, in addition to the structure resulting from this correlation, naturally constrained by the sparse anatomical structure of the *Tg(gad1b:Gal4; UAS:GCaMP6f)* transgenic (which additionally shows some mosaic expression due to UAS).

Fish simulations: PID Controllers

Basic PID (Proportional-Integral-Derivative) Controller

PID controllers[53] are a type of control mechanism found in a variety of scientific and engineering fields used to correct a signal $s(t)$ to a set value S based upon an error function $e(t) = S - s(t)$ by the addition of a control variable $u(t)$. In the most basic PID controller, the control function is an additive function of three terms: the proportional (P), the integral (I), and the derivative (D) terms: $u(t) = K_P e(t) + K_I \int_o^t e(\tau)d\tau + K_D de(t)/dt$, which functions to drive the process to the set value S. In this work, we utilize two formulations of PID controllers (one with bout-like swimming in Figure 1, and another using a continuous approximation to swim output for analytical tractability in Figures S4B–S4F) in order to simulate a fish's swim behavior in response to visual drift.[72,99] These formulations are detailed below.

Figure 1D simulations

To simulate a fish's behavior in various conditions (Figure 1D), we utilize a PID controller, although without a derivative element (i.e., without an acceleration term), and with swim bout-like motor output. The probability of a swim bout at time t is:

$$p(swim(t)) = -\alpha v(t) - \beta \int_o^t v(\tau)d\tau$$

where p was additionally thresholded to lie between 0 and 1 and where α and β are constants controlling the effect of velocity and position, respectively and $v(t)$ is the flow velocity including both passive displacement and swim-induced (closed-loop) motion. In the model fish with no spatial memory (Figure 1D, top) the value of α during the *swim* period was set to 0.022 and the value of β to zero, reflecting the fact that only the fish's perceived velocity, and not the memory of prior position, determines the probability of swimming. In the model fish with spatial memory (Figure 1D, bottom), the value of α was set to 0.01 and the value of β to 0.014, reflecting

the fish's memory of its initial location. In all conditions, the displacement per swim bout was 0.8, with a minimum inter-bout interval of 1 second (30 simulated time units) used in order to approximate the fish's natural swimming behavior. Note that increasing the value of β decreases the time until trajectories from each pre-displacement condition converge. Ignoring the refractory period, the fish without spatial memory can also be viewed as a homogeneous Poisson process with parameter with constant parameter $\lambda = \alpha v$, while the fish with spatial memory will be recognized as a nonhomogeneous Poisson process allowing for a memory of the spatial position.

Figures S4B–S4F simulations

To simulate the PID-style control system of Figures S4B–S4F, we used a simulation in which, for simplicity, model fish were not constrained to swim at random Poisson times, but instead we used a continuous approximation to swimming, $swim(t) = f(-\alpha v_0(t) - \beta \int_0^\infty v(t-t')e^{-t'/\tau}dt')$, where $f(x)=x$ for $x>0$ and $f(x)=0$ otherwise, $v_0(t)$ is the flow velocity, $v(t) = v_0(t) + swim(t)$ is the perceived velocity (positive velocity represents forward movement), and α and β are finite parameters. The proportional term $\alpha v_0(t)$ in the *swim* equation is based on the flow velocity $v_0(t)$ to model a fish that does not immediately react to its own velocity commands; this is a biologically realistic choice because real fish swim in bouts, in between which they move with the flow so they can perceive the pure water flow velocity. This choice also makes the Figures S4B–S4F model consistent with the bout-based Figure 1D model, in which $v_0(t)$ is observed prior to discrete swim bouts. The integral term $\beta\int v(t\text{-}t')e^{-t'/\tau}dt'$ integrates over all perceived velocity (i.e. both flow between swim bouts and self-generated visual motion during bouts). The exponent in the integral represents leaky integration, i.e. a memory with a forgetting time constant τ (this formulation is equivalent to the discrete-time approximation where *new memory* = $(1\text{-}\delta t/\tau)\cdot$*(old memory)* + $\delta t\cdot$*velocity*, from which can be seen that longer time constants τ lead to a longer lasting memory trace).

These equations can be solved to illustrate why gradual positional drift naturally occurs in such control systems. We specifically find the steady-state drift velocity in the case of constant flow (e.g. the fairly constant drift seen at later times in the real data in Figure S4A and the model data in Figures S4B–S4F). We assume the flow is backward and swimming is forward. Since swimming is positive, we can drop the nonlinearity so that $swim(t) = -\alpha v_0(t) - \beta \int_0^\infty v(t-t')e^{-t'/\tau}dt'$. The velocity of the fish in the presence of (water) flow of constant speed v_0 is $v(t) = v_0 + swim(t)$. We assume the fish drift becomes steady (i.e. the swimming becomes steady based on the flow velocity), and once it does, $v(t) = v_{eq} = constant$. This implies that $v_{eq} = v_0 - \alpha v_0 - \beta \int_0^\infty v(t-t')e^{-t'/\tau}dt' = v_0 - \alpha v_0 - \beta \int_0^\infty v_{eq}e^{-t'/\tau}dt' = v_0 - \alpha v_0 - \beta v_{eq} \int_0^\infty e^{-t'/\tau}dt' = v_0 - \alpha v_0 - \beta v_{eq}\tau$, which can be solved for the steady state velocity, $v_{eq} = \frac{(1-\alpha)v_0}{1+\beta\tau}$. Thus there are certain conditions under which the steady state velocity can be zero: either the virtual water flow velocity is zero ($v_0 = 0$), or the memory is perfect ($\tau = \infty$), or α is perfectly tuned (to 1). All three of these conditions would be unrealistic in biological systems; in more realistic scenarios there tends to be positional drift when there is a steady flow, even when positional memory is precise.

Fish location decoding from SLO-MO activity

To decode a fish's virtual position from its brain activity in response to a pseudo-random motion stimuli encompassing both open-loop (where the fish was not in control of its motion in VR) as well as closed-loop (where the fish actively controlled its location in VR) periods, we utilized a ridge regression with a leave-one-out cross validation (LOOCV) paradigm. For each trial, we set the fish's position to zero prior to the beginning of the open-loop pre-displacement period and integrated the velocity for both open-loop pre-displacement, delay, and closed-loop swim periods prior to down-sampling the position to the acquisition rate of the brain imaging data, yielding position traces as seen in Figure 4F. Each trial was then sequentially excluded from a training set, where we fit a linear decoder to the equation:

$$\hat{p}(t) = \sum_{i=1}^{n} w_i a_i(t)$$

where w is the parameter weight, $a(t)$ is the activity at time t, and i is a subscript for each neuron. Note that in the decoding the true position is offset by one time point (~300 ms) relative to the decoded position to account for delayed calcium responses, and a baseline corresponding to the first time point at each trial is subtracted from the trial's activity. To avoid overfitting and issues with multicollinearity, we regularized the fit using a ridge regression. We repeated the regressions multiple times, setting the value of the regularization constant λ from 0.5 to 50 in steps of 0.5 and computing the RMSE between the testing trials' true and estimated positions for each selected value of λ. The value of λ minimizing the average RMSE was then selected independently across fish.

Motosensory gain adaptation simulation

To simulate behavior with motosensory gain adaptation but without positional integration (Figure S1K, green and magenta dashed lines), we assumed that fish would linearly adjust swim vigor over a period of 5 seconds from [original swim vigor] to the optimally-adjusted swim vigor under the new gain, which is [original swim vigor]×[original motosensory gain]/[new motosensory gain]. For example, if the original swim vigor is 1 and the original motosensory gain is 1 but then changes to a new motosensory gain of 2, the model assumes that fish will linearly shift its swim vigor from 1 to 0.5 over a period of 5 seconds. The approximately 5-second period of adaptation is assumed based on previous observations of the speed of adaptation following motosensory gain changes.[51,63] This model produces a parabolic position trajectory (because [fish velocity] = [drift velocity] + [swim vigor]×[motosensory gain]) as shown in Figure S1K.

QUANTIFICATION AND STATISTICAL ANALYSIS

Data were tested for statistical significance across fish by, as indicated in the text and figures/legends,

- Two-tailed paired t-test (Figures S1G–S1J, S1L, S7H, S7J, and S7P)
- One-way ANOVA followed by Tukey's post-hoc test (Figure S7L)
- Wilcoxon rank-sum test (Figure 6J)
- One sample t-test (Figures 1F, 1H, 5E, 5H, S1E, S7N, and S7O)
- Shuffle test (Figures 2D–2F)
- Pearson regression (Figures 4G and 4H)

Details including numbers are specified in the text and figure legends. Error bars in figures represent SEM unless otherwise stated. All the statistical analyses were performed using custom-written scripts in Python. Distribution of all population data first went through a normality test, and the Wilcoxon rank-sum test was used if the data were not normally distributed.

CellPress
OPEN ACCESS

Supplemental figures

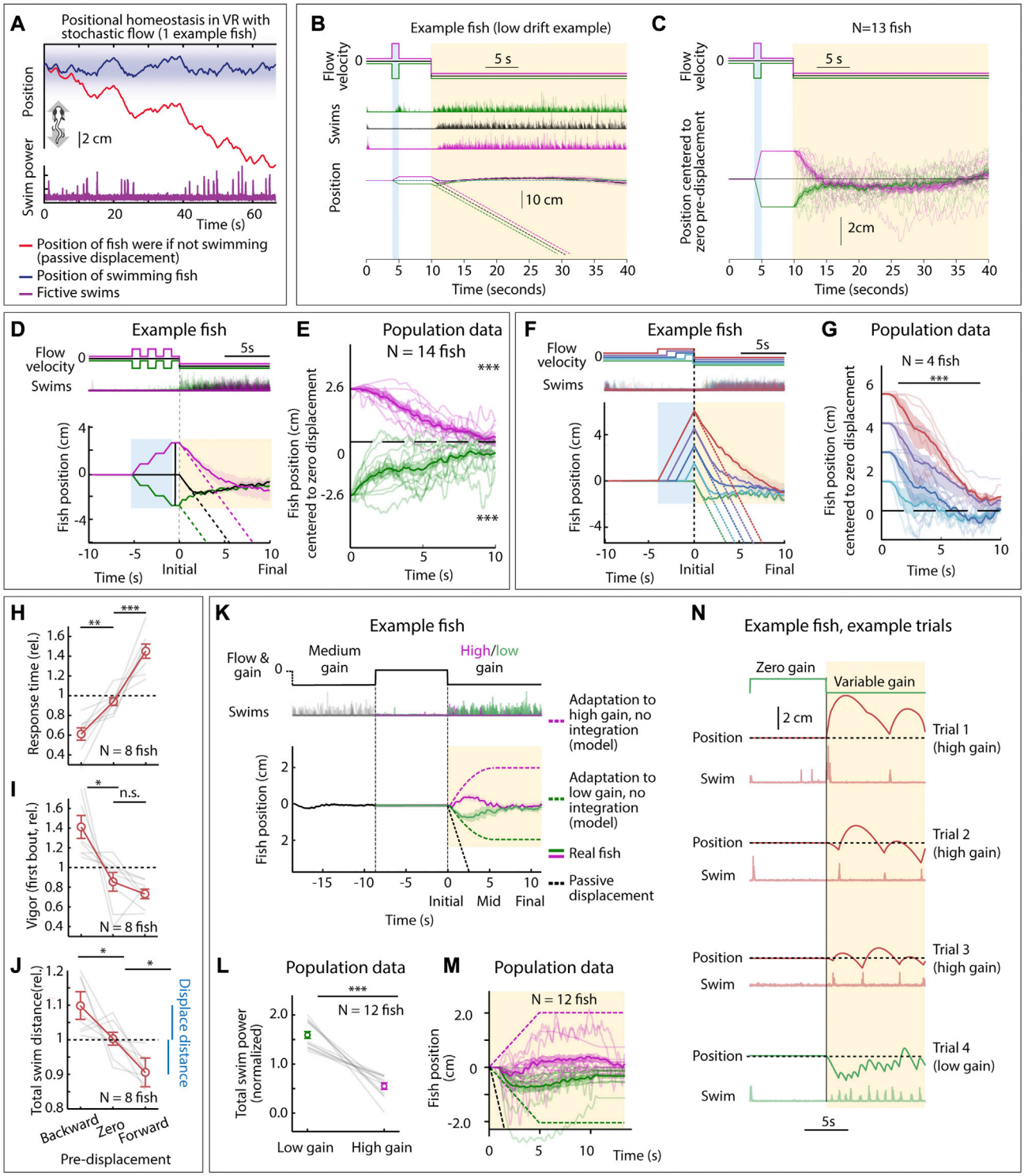

(legend on next page)

Figure S1. Positional homeostasis, extended characterization, related to Figure 1

(A) Positional homeostasis example, in which an example fish approximately stabilizes its location in a stochastic virtual water current.

(B) Positional homeostasis assay with a 30-s swim period in an example fish.

(C) Centered trajectories for N = 13 fish showing persistent convergence.

(D) Triple forward pre-displacement/backward pre-displacement assay. Example fish, showing converging trajectories, indicating successful integration across three consecutive pre-displacements. (Shaded regions: SEM in all panels.)

(E) Population data (14 fish) showing near-complete correction for earlier pre-displacement. (One-sample t test, ***$p < 0.001$, $p = 9.7e{-}10$ for forward pre-displacements, $p = 1.9e{-}10$ for backward pre-displacement. Error bars: SEM in all panels.)

(F) Assay to test integration over varying durations. An example fish successfully integrates pre-displacement and corrects for it in the swim period.

(G) Population data (4 fish) showing accurate correction, i.e., path integration. (Two-tailed paired t test, ***$p < 0.001$, $p = 1.08e{-}7$ for all forward pre-displacements.)

(H) Animals respond faster (slower) after a backward (forward) pre-displacement, consistent with Figure 1F. (Two-tailed paired t test, **$p < 0.01$, $p = 1.76e{-}3$ for backward pre-displacement, ***$p < 0.001$, $p = 3.1e{-}4$ for forward pre-displacement.)

(I) Animals respond more vigorously after a backyard pre-displacement, consistent with Figure 1F. (Two-tailed paired t test, *$p < 0.05$, $p = 0.0151$ for backward pre-displacement, n.s. $p > 0.05$, $p = 0.115$ for forward pre-displacement.)

(J) Total swim distance (normalized) corresponds to the earlier pre-displacement, consistent with Figure 1F. (Two-tailed paired t test, *$p < 0.05$, $p = 0.031$ for backward pre-displacements, and $p = 0.012$ for forward pre-displacements.)

(K) After motosensory gain changes (high: ×1.5, low: ×0.5), animals still integrate position. Dashed lines: position of model fish performing gain adaptation (linear adjustment of vigor over 5 s) but no path integration. Solid lines: position of real fish.

(L) Swim vigor during low or high motosensory gain shows gain adaptation. (Two-tailed paired t test, ***$p < 0.001$, $p = 1.6e{-}5$.)

(M) Average fish position in low versus high gain trails initially diverges, then converges. Dashed lines: normalization to model fish performing gain adaptation but no path integration.

(N) Example trials during high and low motosensory gain (data from K–M) showing accurate positional homeostasis in both cases.

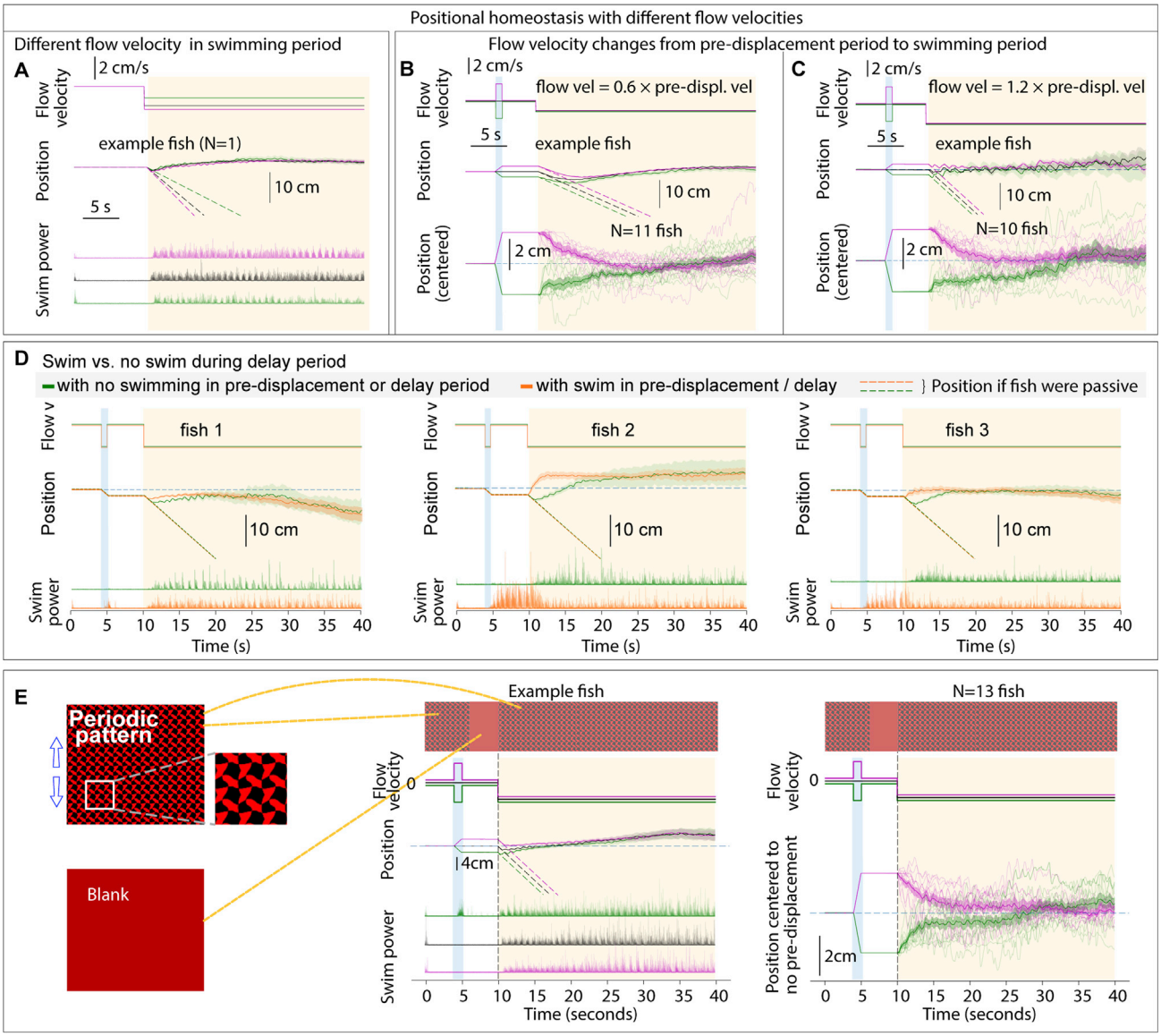

Figure S2. Additional features of positional homeostasis, related to Figure 1

(A) Trajectories of an example fish swimming against different flow velocities in the swim period.

(B and C) Behavior when flow velocity in the swim period is lower or higher than that in the pre-displacement period.

(D) Swimming in the pre-displacement or delay periods does not influence eventual fish location, i.e., fish track the visual stimulus and use integrated visual flow.

(E) Stimuli used to test if visual flow is sufficient for positional homeostasis. The periodic pattern looks the same when translated by an integer number of finely spaced periods. During the pre-displacement period, the fish transitions an integer number of periods. In the delay period, the screen becomes blank to additionally test whether animals are locking on to a specific feature of their environment. In the swim period, the pattern becomes visible again. Single-fish and population data shows convergence, i.e., positional homeostasis can be based only on integrated visual flow.

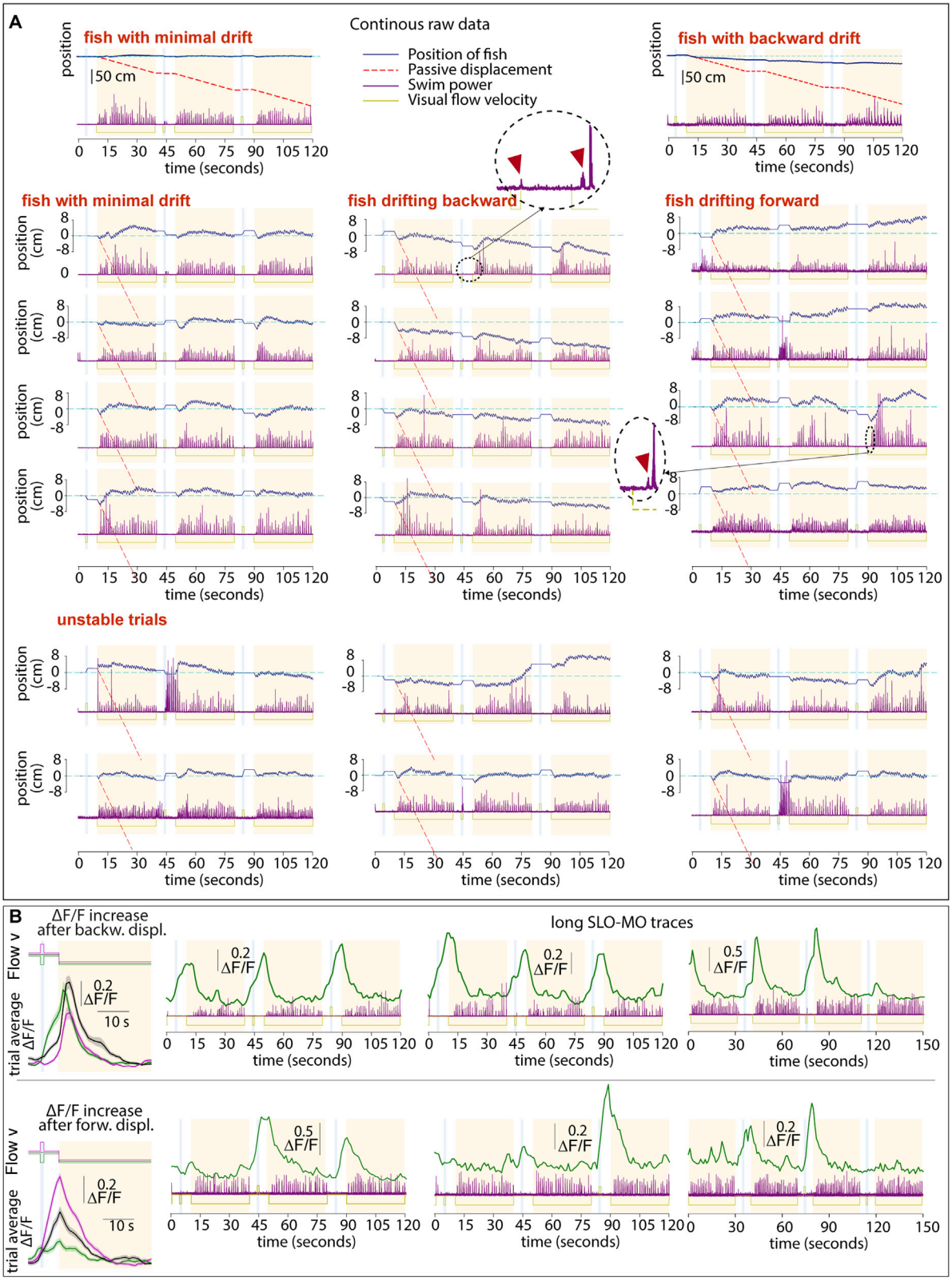

(legend on next page)

Figure S3. Examples of single, non-averaged trials, related to Figure 1

(A) Trajectories of three example fish (see Figure S4A for average trajectories of those and other fish). Trials are consecutive in groups of three, stacked vertically. For visualization, the start of the first of each triplet is shifted to zero. Little fictive "probe swims" are visible and magnified in the dashed circles; these probe swims are often present right after the start of a backward pre-displacement and at the start of swim periods and may inform the fish that it's in an open-loop (pre-displacement) or closed loop (swim) period. We hypothesize that the probe swim in the pre-displacement may reduce subsequent swim attempts in the pre-displacement and delay periods, whereas in the swim period it may enhance further closed-loop swimming. In these fish, slow drift is present that can be minimal (left fish), backward (middle fish), or forward (right fish), i.e., positional homeostasis is not perfect. Figure S4A quantifies this drift and Figures S4B–S4F proposes an explanation in a control theory framework. The lower two rows illustrate "unstable trials," showing that swimming behavior is variable and likely driven not only by visual flow but also other factors (e.g., fluctuating "internal states," "noise," etc.).

(B) Single-trial SLO-MO activity traces during 6.5 min of data for two example neurons with different tuning properties in one fish.

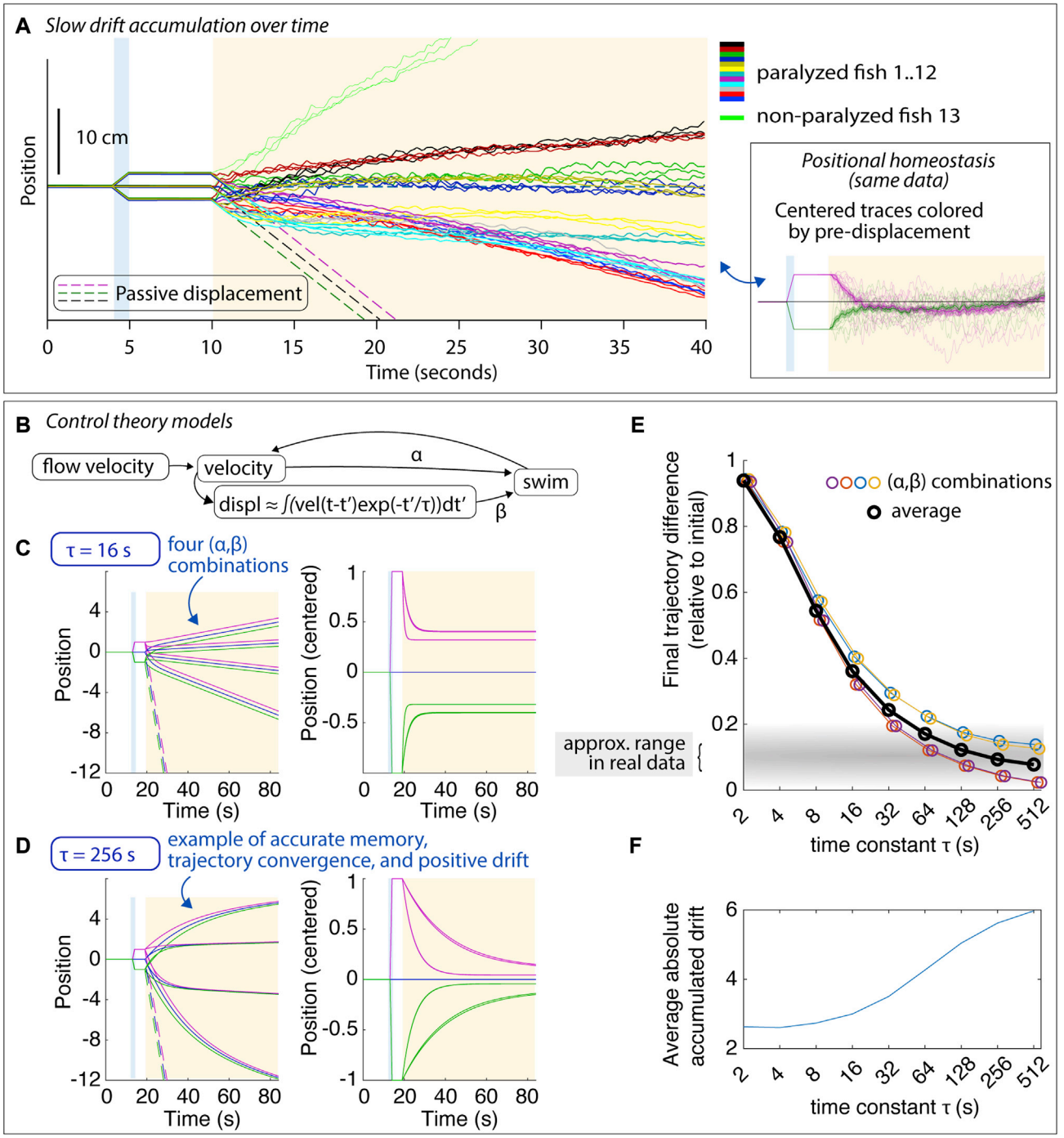

Figure S4. Drift in positional homeostasis and PID control theory, related to Figure 1

(A) Average trajectories showing drift in the swim period that can be slowly forward or slowly backward or minimal. Fish were not imaged. When fish were imaged and exposed to blue light-sheet laser light, drift tended to be larger. One unparalyzed fish was tested; this fish drifted forward. Despite the drift, average trajectories converged for every fish; average trajectories are shown in the same color for each fish for each of the three possible pre-displacements, with the different pre-displacements shown in distinct colors in the inset and in Figure S1C.

(B) Diagram of PID control system (see STAR Methods). Swimming is modeled as a continuous variable, a weighted linear combination of a velocity term and a displacement term, and constrained to be non-negative. The displacement term is a leaky integral of fish velocity with memory time constant τ.

(C) Example trajectories during simulated behavior with τ = 16 s for four (α,β) combinations, shown as raw position (left) and centered to the no-displacement trajectory (right). For this short time constant, trajectories converge only about halfway.

(legend continued on next page)

(D) For a longer memory time constant τ = 256 s, trajectories converge much more. Importantly, trajectories can drift forward or backward despite the fact that positional memory is quite accurate.
(E) For the four (α,β) combinations, the final trajectory difference is mainly a function of the memory time constant. In the real data, trajectories converge within about 5%–20%, suggesting a memory time constant of about a minute or more (gray shaded area).
(F) The average accumulated absolute drift over (α,β) pairs.

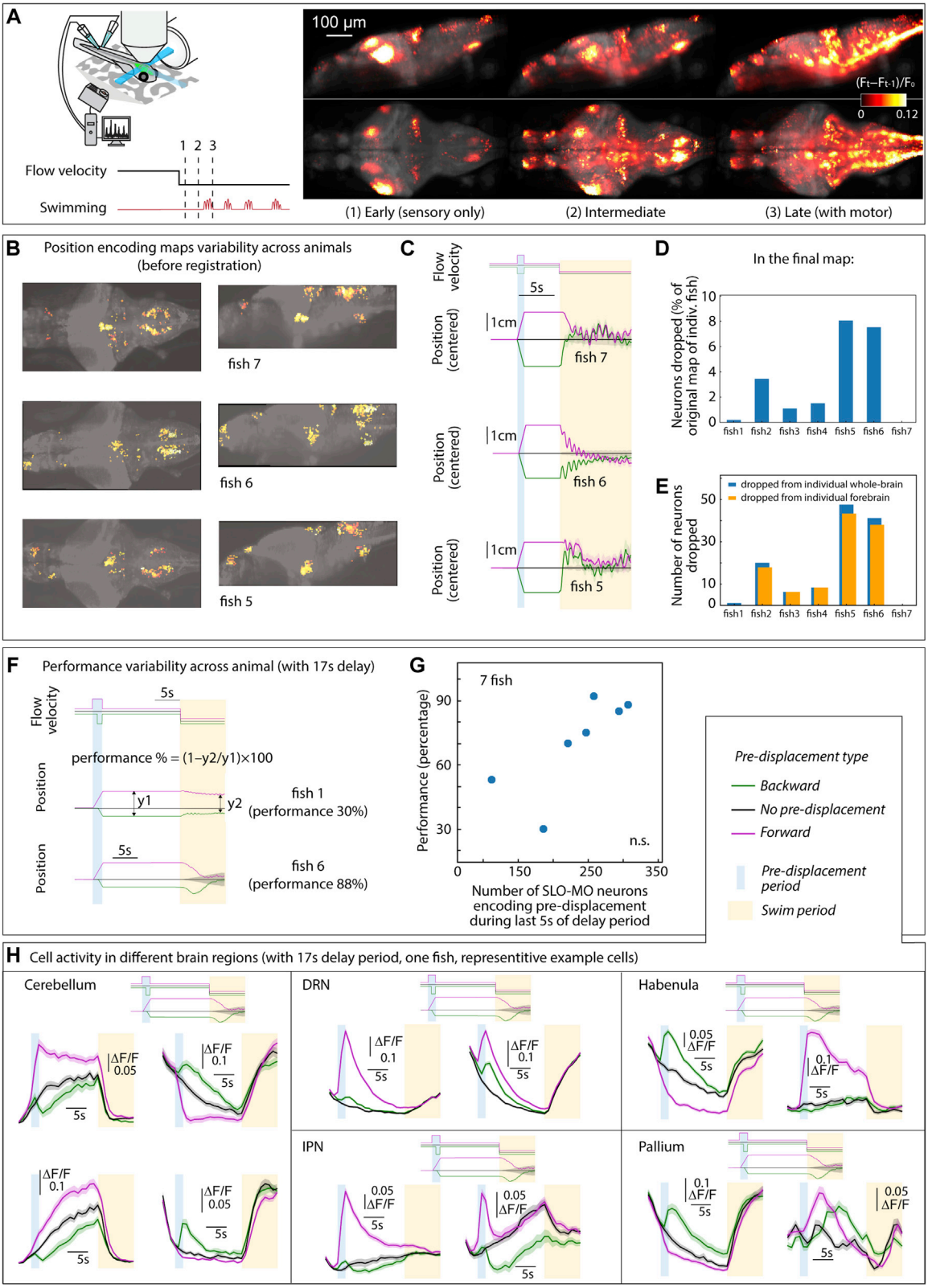

(legend on next page)

Figure S5. Positional homeostasis activity and variability, related to Figure 2

(A) Brain activity averaged over trials in an example fish shown as changes over time $(\Delta F/F)_{t-1}$ and $(\Delta F/F)_t$. Left: in the 300 ms following onset of backward flow through VR (forward visual motion from the point of view of the fish). Middle: at an intermediate time, after stimulus onset, just before (0–300 ms) swim onset. Right: immediately following (0–300 ms) swim onset.

(B) Examples of functional brain maps for individual fish before combining them into the final map in Figure 2D.

(C) With a 5 s delay period, fish perform positional homeostasis with little variability.

(D and E) Percentage of neurons dropped from each animal was small, and that the majority of these neurons resided in the forebrain.

(F and G) With a 17 s delay period, the number of SLO-MO neurons encoding the displacement memory appears to correlate to positional homeostasis performance, although the sample size is too small to be significant.

(H) Persistent positional encoding signals were detected in different brain regions, cerebellum, dorsal raphe nucleus, area of the interpeduncular nucleus, habenula, and pallium.

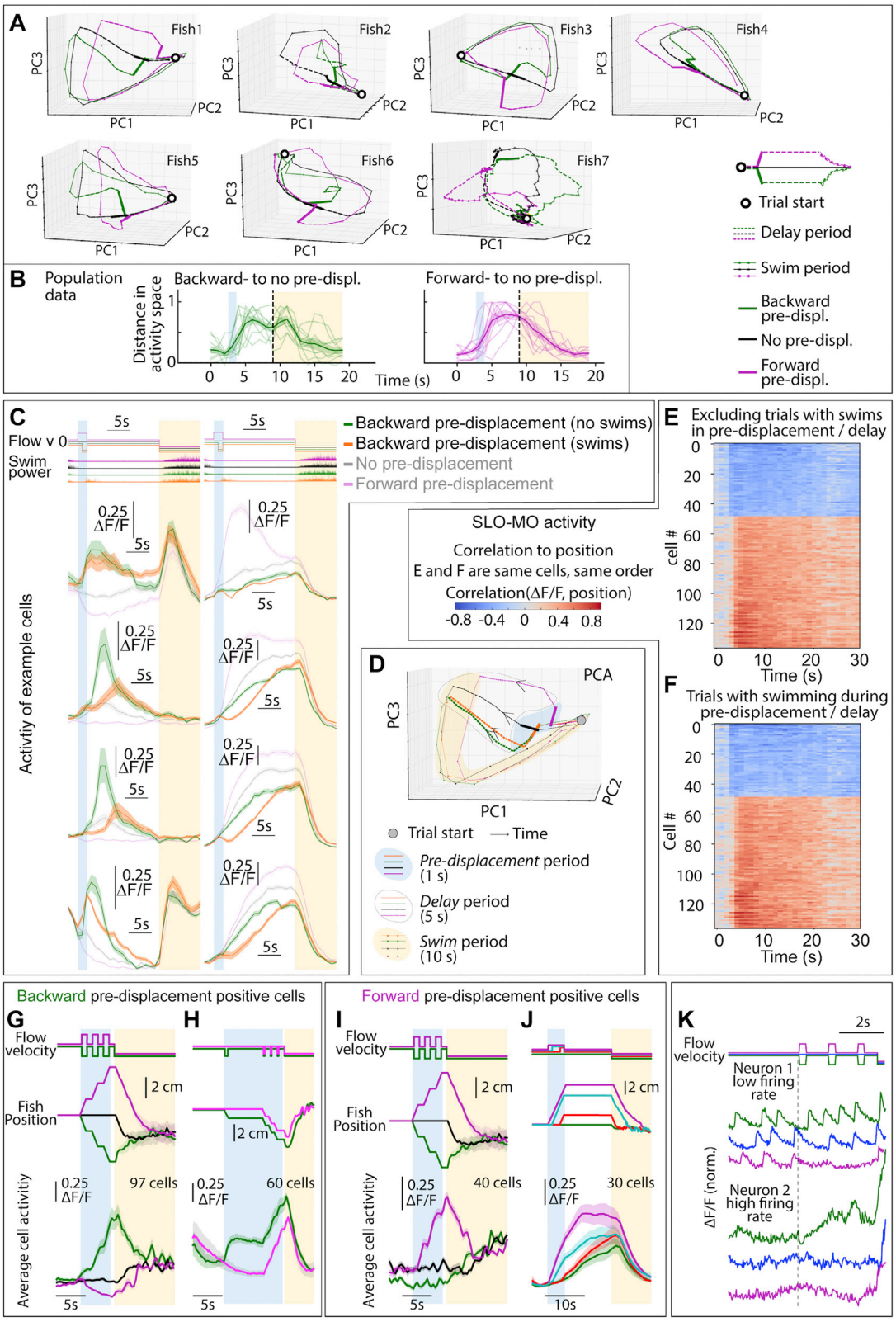

(legend on next page)

Figure S6. Further characterization of SLO-MO activity, dependence on complex trajectories and swimming, related to Figure 3

(A) Trajectories through dimensionally reduced network space for seven individual fish, related to Figure 3. Dimensionality reduction done with principal-component analysis (PCA).

(B) Distance in PC space (first 3 components) between backward pre-displacement and zero pre-displacement, and forward pre-displacement and zero pre-displacement activity, for 9 fish. Since distances are zero or greater, noise causes distance to always be positive even before the pre-displacement at ~2 s. (Shaded regions: SEM.)

(C and D) SLO-MO cells showed a transient decrease in activity during swimming, after which they returned to activity levels encoding past displacements.

(E and F) Ranked correlation of cell activity to fish position for example fish of Figures 3B and 3C separated by trials with and without swimming in pre-displacement and delay periods.

(G) Neurons (in an example fish) with increasing activity following three consecutive backward or forward pre-displacements, showing integration. (Shaded regions: SEM in all panels.)

(H) Neurons (in an example fish) showing integration over backward pre-displacements. The green trials are offset by one additional displacement 5 s before the triplet displacement; this is reflected in a persistent increase in neuronal activity.

(I) Integration across triplet displacements by neurons that respond positively to forward displacements.

(J) Additional example of integration by SLO-MO neurons during forward pre-displacements of varying durations followed by delay periods.

(K) Individual neuron traces showing integration across triplet pre-displacements, fast imaging of single planes at 33 Hz. The firing rate of neuron 1 is low enough that individual spikes are visible in the calcium trace, showing persistently increasing spike rate after backward pre-displacements and persistently decreasing spike rate after forward pre-displacements. The firing rate of neuron 2 appears to be higher and, although individual spikes are not visible due to sampling rate and calcium indicator limitations, firing rate can be seen to increase following a backward pre-displacement relative to a forward pre-displacement.

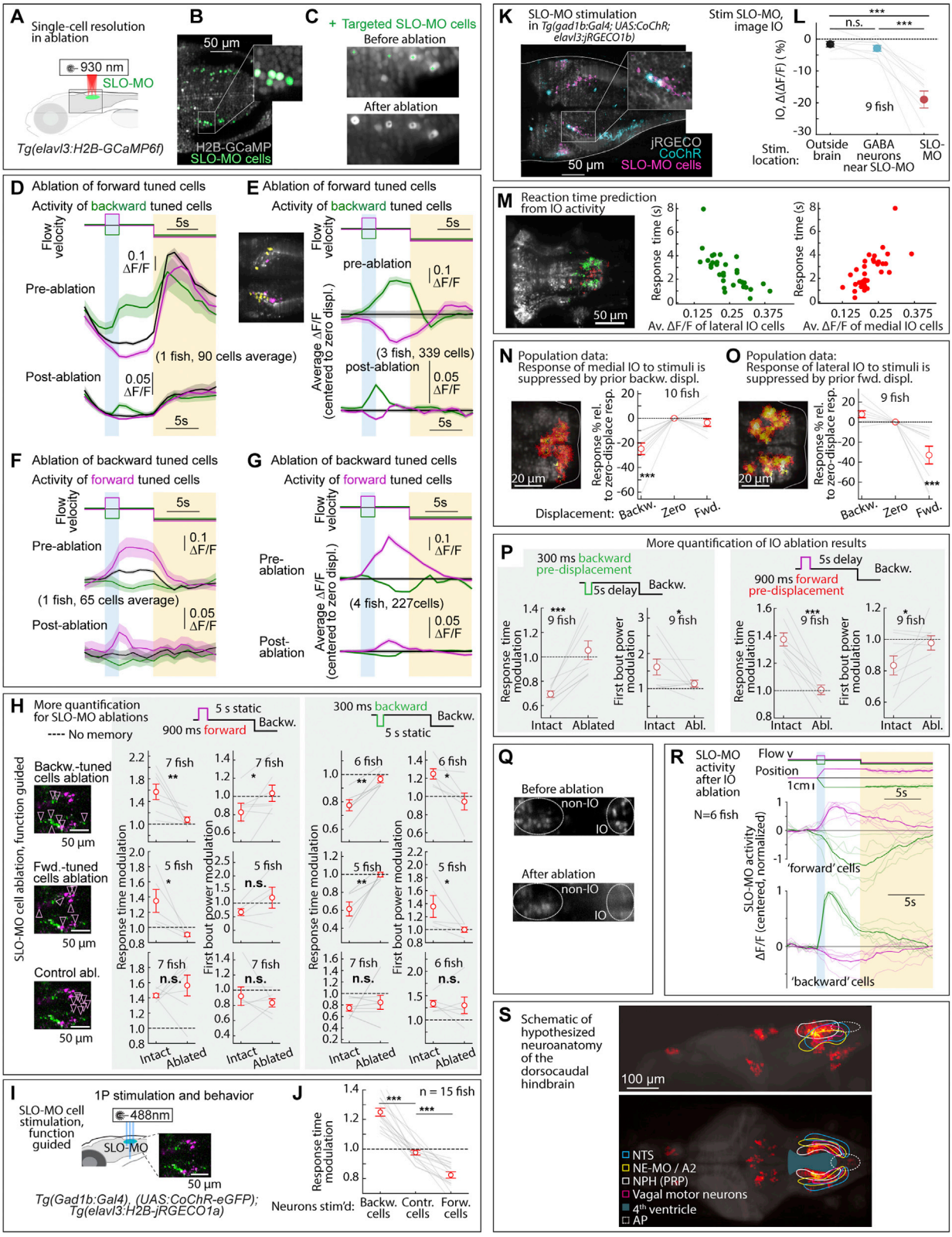

(legend on next page)

Figure S7. Additional ablation and stimulation results, and dorsocaudal hindbrain anatomy, related to Figures 2, 5, and 6

(A) Ablation setup for ablating functionally identified SLO-MO populations using a two-photon laser and *Tg(elavl3:GCaMP6f)* fish.

(B and C) Calcium imaging of functionally identified and targeted SLO-MO cells before and after two-photon ablation showing single-cell precision.

(D) SLO-MO cells (of one example fish) whose activity increases after backward pre-displacement, before and after ablation of SLO-MO cells whose activity increases after forward pre-displacement. A sensory response remains, but persistence is abolished.

(E) Population data, similar to (D), showing the loss of persistent activity but preservation of sensory responses across 3 fish. Inset: example single imaging plane showing some spatial intermingling of forward-tuned SLO-MO cells (magenta) and backward-tuned SLO-MO cells (yellow).

(F and G) Similar to (D) and (E), but showing activity of forward-tuned cells before and after ablation of backward-tuned cells, again showing the loss of persistence but preservation of sensory responses.

(H) Additional quantification of the effects of SLO-MO ablation. Ablation of backward-tuned cells, ablation of forward-tuned cells, and control ablations are shown. (Two-tailed paired t test, $^{**}p < 0.01$, $^{*}p < 0.05$, n.s. $p > 0.05$. Error bars: SEM in all panels.)

(I) Diagram of optogenetic stimulation and functional imaging setup.

(J) Optogenetic excitation of functionally identified SLO-MO neurons causes changes in the time to first swim bout in the swim period, consistent with changes in distance swum shown in Figures 5G and 5H. (Two-tailed paired t test, $^{***}p < 0.001$.)

(K) Functionally identified SLO-MO neurons in *Tg(gad1b:Gal4; UAS:CoChR; elavl3:jRGECO1b)* fish from the *elavl3:jRGECO1b* red channel overlaid with the *gad1b:Gal4; UAS:CoChR* green channel. Single-cell specificity is obtained by sparse expression of CoChR (using the Gal4-UAS system) and stimulation with a high-resolution DMD setup.[123]

(L) Optogenetic stimulation of SLO-MO neurons (one neuron at a time of any functional type; hence no significant integration expected) causes inhibition of specific IO neurons (population data). Stimulation of CoChR-positive non-SLO-MO neurons causes no significant IO response. ($p = 1.7e{-}7$ by one-way ANOVA, 9 fish. $^{***}p < 0.001$, by Tukey's post hoc test. Same data as Figure 2K. Shaded regions and error bars: SEM in all panels.)

(M) Correlation between lateral and medial IO activity and reaction time, complementing the joint decoder of Figure 6G.

(N and O) Backward displacements suppress medial IO activity; forward displacements suppress lateral IO activity. Population data to complement Figures 6A–6D. (One-sample t test, $^{***}p < 0.001$.)

(P) Additional quantification of effects of IO lesions on response time and swim power. (9 fish, two-tailed paired t test, $^{***}p < 0.001$, $^{*}p < 0.05$. Error bars: SEM in all panels.)

(Q) Calcium imaging of IO neurons using *Tg(elavl3:H2B-GCaMP6f)* fish before and after IO ablation.

(R) Persistent SLO-MO activity encoding self-location remains intact after ablation of IO cells.

(S) Known and hypothesized neuroanatomy of the dorsocaudal larval zebrafish hindbrain. This schematic, based on multiple zebrafish and mouse publications and atlases, accompanies the hypothesis that SLO-MO overlaps with the homolog of the nucleus prepositus hypoglossi (NPH), a major GABAergic input to the IO.[94,95] SLO-MO neurons are also GABAergic and project to and inhibit the IO. Our results are consistent with a monosynaptic connection between SLO-MO and IO, and we showed that activating SLO-MO functionally inhibits IO. SLO-MO neurons are spatially arranged relative to the nucleus of the solitary tract (NTS), noradrenergic area A2[96] (called NE-MO in Mu et al.[52]), and are close to the fourth ventricle[97]; the NPH also has these properties (Allen Mouse Brain Atlas, http://www.brain-map.org [93]). Historically, the NPH has been studied in the context of eye movement control, but (parts of) the NPH may be multifunctional. Circuits for positional homeostasis and for oculomotor control have in common that they must integrate visual slip into a persistent signal,[124–126] so the possibility exists that these circuits showed some overlap, possibly with similar mechanisms for persistent activity.